ARL

US Army Research Laboratory

Material Models for the Human Torso Finite Element Model

by Carolyn E Hampton and Michael Kleinberger

NOTICES

Disclaimers

The findings in this report are not to be construed as an official Department of the Army position unless so designated by other authorized documents.

Citation of manufacturer's or trade names does not constitute an official endorsement or approval of the use thereof.

Destroy this report when it is no longer needed. Do not return it to the originator.

US Army Research Laboratory

Material Models for the Human Torso Finite Element Model

by Carolyn E Hampton
Oak Ridge Institute for Science and Education (ORISE), Belcamp, MD

Michael Kleinberger
Weapons and Materials Research Directorate, ARL

REPORT DOCUMENTATION PAGE

Form Approved
OMB No. 0704-0188

1. REPORT DATE *(DD-MM-YYYY)*	2. REPORT TYPE	3. DATES COVERED (From - To)
April 2018	Technical Report	18 September 2017–9 February 2018

4. TITLE AND SUBTITLE

Material Models for the Human Torso Finite Element Model

5a. CONTRACT NUMBER

1120-1120-99

5b. GRANT NUMBER

5c. PROGRAM ELEMENT NUMBER

6. AUTHOR(S)

Carolyn E Hampton and Michael Kleinberger

5d. PROJECT NUMBER

5e. TASK NUMBER

5f. WORK UNIT NUMBER

7. PERFORMING ORGANIZATION NAME(S) AND ADDRESS(ES)

US Army Research Laboratory
ATTN: RDRL-WMP-B
Aberdeen Proving Ground, MD 21005-5069

8. PERFORMING ORGANIZATION REPORT NUMBER

ARL-TR-8338

9. SPONSORING/MONITORING AGENCY NAME(S) AND ADDRESS(ES)

10. SPONSOR/MONITOR'S ACRONYM(S)

11. SPONSOR/MONITOR'S REPORT NUMBER(S)

12. DISTRIBUTION/AVAILABILITY STATEMENT

Approved for public release; distribution is unlimited.

13. SUPPLEMENTARY NOTES

14. ABSTRACT

Behind-armor blunt trauma (BABT) is a current research topic because of increased interest in lightweight armor. A finite element analysis was performed to improve the biofidelity of the US Army Research Laboratory (ARL) human torso model in preparation for simulating blunt chest impacts and BABT. The overly stiff linear elastic material models for the torso were replaced with material characterizations drawn from current literature. Biofidelity of the ARL torso was determined by comparing peak force, force-displacement, peak compression, and energy absorption data with cadaver responses to a 23.5-kg pendulum impacting the chest center at 6.7 m/s. Nonlinear foam, viscous foam, soft rubbers, fibrous hyperelastic rubbers, and low moduli elastic material were considered as material models for the flesh, organs, and bones. Simulations modifying one tissue type revealed that the flesh characterization was most crucial for predicting compression and force, followed closely by the organs' characterizations. Combining multiple tissue modifications allowed the ARL torso to mimic the cadaveric torsos by reducing peak force and increasing chest compression and energy absorption. Limitations imposed by the Lagrangian finite element approach were discussed with potential workarounds described. Proposed future work was split between considering additional impact scenarios accounting for position and biomaterial variability.

15. SUBJECT TERMS

chest, torso, biomechanics, behind-armor blunt trauma, blunt injury, finite element, organs, soft tissue, material models, human body modeling, LS-DYNA

16. SECURITY CLASSIFICATION OF:			17. LIMITATION OF ABSTRACT	18. NUMBER OF PAGES	19a. NAME OF RESPONSIBLE PERSON
			UU	68	Carolyn E Hampton
a. REPORT	b. ABSTRACT	c. THIS PAGE			19b. TELEPHONE NUMBER (Include area code)
Unclassified	Unclassified	Unclassified			410-306-2983

Contents

List of Figures

List of Tables

Acknowledgments

INTENTIONALLY LEFT BLANK.

1. Introduction

Behind-Armor Blunt Trauma (BABT) represents a category of injuries induced by the back face of chest armor in response to nonpenetrating projectile impacts. BABT can result in significant thoracic and abdominal injuries such as those observed in law enforcement officers wearing commercial flexible body armor (Cannon 2001). Recent interest in lightweight armor requires the capability to accurately assess injury risk to maintain adequate levels of protection.

The noninjury threshold for back-face deflection was previously limited to 44 mm based on research performed on behalf of the Departments of Justice and Defense (Hanlon and Gillich 2012). This standard was developed from decades of data, including ballistic shots at armor-wearing animals (Goldfarb et al. 1975) and ballistic range testing of armors with various backings (Prather et al. 1977). This limit was also codified as the standard for soft armors as described in the National Institute of Justice (NIJ) Standard 0101.06 (Mukasey et al. 2008).

The previous 44-mm standard for body armors required ballistic tests of armor backed by Roma Plastilina clay. The scope has expanded to include hard armors as well. The validity of the 44-mm limit has been questioned on multiple fronts (Hanlon and Gillich 2012). Criticisms include that the limit is overly conservative since few injuries have been observed in the goat tests and in the field (Carr et al. 2016), that variations in human sizes and ballistic conditions were not fully considered, and that the connections between the clay-backed deflections and goat lethality were preliminary results. Recently there has been interest in increasing the deflection limit to accommodate lighter armor (GAO 2017).

In the past, new sets of experiments would be required to demonstrate compliance with new design standards. Advances in computational power have allowed a new method of injury evaluation to flourish. The finite element (FE) approach offers the ability to simulate both the NIJ Standard ballistic tests (Bass et al. 2006) or to directly model the human response to ballistic impact (Kroell 1994). Computational studies have already been used to evaluate the armor performance on alternative species such as canines (Stojsih 2015) and for fifth percentile size human females (Merkle et al. 2008). Information that would be difficult to obtain experimentally, such as internal pressures and displacements, are accessible through simulation.

FE models are typically validated against controlled experiments before use in applications. This study examines material characterizations and parameters in a FE model of the human torso in preparation for simulating BABT. The intent to

demonstrate that the torso model provided a realistic response with results comparable to physical experiments to support future efforts to evaluate BABT.

2. Methods

2.1 Review of Experimental Data

Kroell et al. (1994) studied the response of the human chest to blunt impact using unembalmed postmortem human subjects (PMHSs) that had been refrigerated less than or equal to 10 days. This study was a subset of a larger body of work (Kroell 1994). The test setup, shown on the left in Fig. 1, shows the seated posture prior to impact. No constraints were placed upon the body. The total chest compression was measured by video tracking the distance between the impactor marker and a marker glued to the specimen's back. The impactor force was measured with a triaxial load cell. Only the horizontal axis component was used in this study. Off-axis load cell curves in the supplemental data were under 100 lb_f, whereas most primary axis forces were in the range of 800–1200 lb_f. In some tests, the heart and aorta were sealed and pressurized to approximately 100 mmHg, and the vascular pressure during impact was measured.
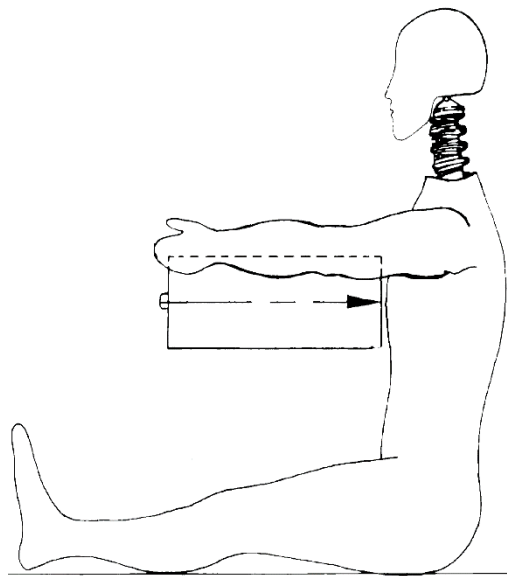
Fig. 1   Schematic of the test setup as applied to PMHS or anthropomorphic test dummies (GPO 2011)

A total of 15 PMHS specimens were tested. Of these, 9 tests used the same impact conditions: a 6-inch (152.4-mm)-diameter impactor, weighing 50.4–52.0 lb (22.9–23.6 kg), with an initial velocity of 15.0–16.6 mph (6.7–7.4 m/s). Impact locations were centered on the chest at the height of the fourth rib interspace. Chest

compression ranged from 2.8 to 4.3 inches (71 to 109 mm). The force-deflection response and fractures documented at autopsy varied between individuals, with age noted as a particularly influential predictor of injury. Two of the tests used 19- and 29-year-old male PMHS; the autopsies revealed no rib injury, no organ injury, and only one sternal fracture. The other 7 tests used mixed male and female PMHS of 60+ years of age, and autopsies revealed organ damage, sternal fractures, and more than 10 rib fractures for most specimens.

This study aims to evaluate the injury potential for a younger (20–30 years old), primarily male population. Thus, the 2 younger male specimens, 19FM and 20FM, were selected as the best tests to use as benchmarks for the US Army Research Laboratory (ARL) torso FE model. The lack of documented injuries was beneficial for a preliminary model evaluation to defer the complexity of fracture prediction and propagation to a later time. Both tests included cardiac vascular re-pressurization, although the data were not used for this study. The primary quantities measured in the PMHS experiments, impactor force and chest compression, were used because the data were readily available in the FE model. The relevant time histories are shown in Fig. 2.
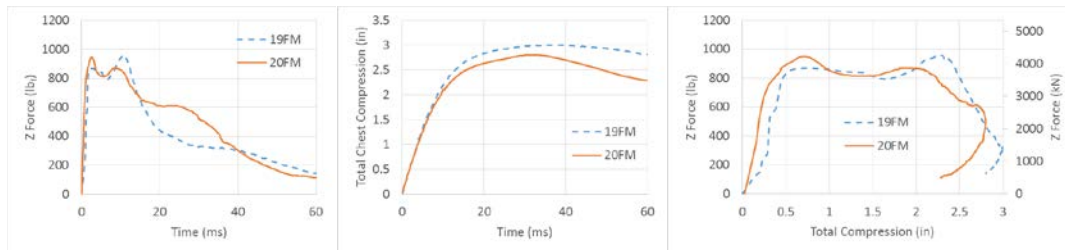
Fig. 2   Impactor Z axis force-time (left), total chest compression-time (center), and force-displacement (right) histories for PMHS tests 19FM and 20FM

2.2 ARL Torso Model

This study used the ARL torso FE model. The FE mesh was created from a human geometric surfaces database (Zygote Media Group Inc. 2015) based on computed tomography (CT) scans of a 50th percentile human male, 21 years old. The torso model contained 271 individually meshed parts held together with ligaments (beam elements) and contacts automatically generated by a custom C++ script. The model is shown in Fig. 3, and the individual parts are described in the Appendix. Further details on the mesh generation and assembly script are described in the previous literature (Sokolow 2015). The entire ARL torso model weighed 30.7 kg (67.7 lb).
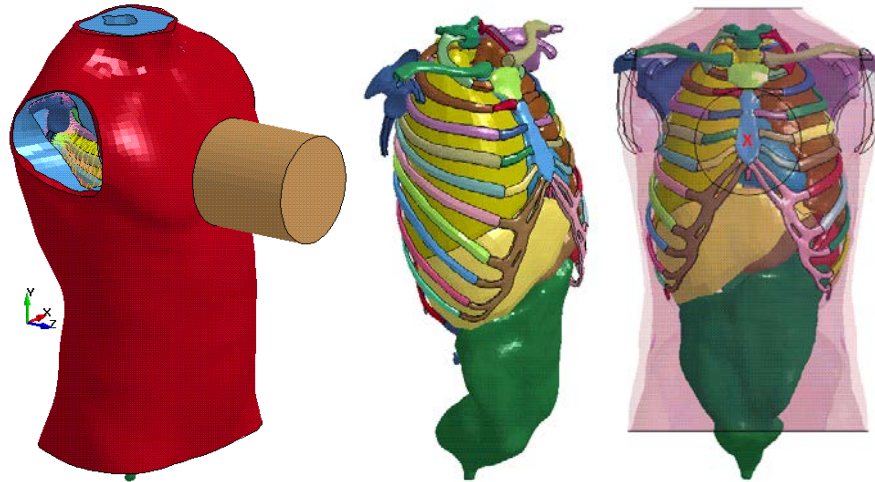
Fig. 3 **Full ARL torso model (left); model with flesh, impactor, and skin hidden (middle); frontal view with transparent impactor, flesh, and skin to show center of impact location (right). All colors randomly assigned to improve contrast.**

Inter-part penetrations were prevented by both ligaments and 645 part-to-part sliding or tied contact interfaces. All parts were initially assigned generic linear elastic (Mat1) material definitions. These materials crudely approximated the tissue properties and were used as placeholders to support the material optimization performed in this study. All parts were assigned 1 of 6 material classes with material properties as shown in Table 1. All beam elements were defined with a 1.128-mm-diameter uniform circular cross section.

Table 1   Linear elastic material models for ARL torso finite element model

Material	Density (kg/m^3)	Modulus (MPa)	Poisson's ratio
Vertebral discs	1,000	280	0.48
Homogenized bone	1,400	1,500	0.42
Organs, flesh, ligaments	1,000	180	0.47
Skin	1,000	10	0.49
Costal cartilage	1,000	400	0.49
Steel cylinder	8,500	200,000	0.30

The impactor was modeled as a 152.4-mm (6-inch)-diameter steel cylinder to match the test setup used by Kroell et al. (1994). The impactor depth was also 152.4 mm (6 inches) and the mass was 23.51 kg (51.8 lb). The height of the impactor was aligned with the middle height of the fourth rib interspace at the intersection with the sternum. The exact location is highlighted with a red X in Fig. 3. The impactor was assigned an initial velocity of –6.7056 m/s (15.0 mph) along the Z axis to match the initial conditions from the experimental tests. For reference, the coordinate

system for all simulations is shown in Fig. 3. Constraints were added to the impactor to prevent all rotations and lateral (X and Y axis) motions.

Chest compressions, both skeletal and total, were measured using the points shown in Fig. 4. Five points in the sagittal plane and along the travel direction of the impactor were selected: the impactor, surface of the chest, back of the sternum, back of the sixth thoracic vertebral process, and the exterior surface of the back. However, the curvature of the back meant that the last point was not visible when the whole torso was viewed from the side. A sixth point on the shoulder was added at the same height but laterally offset to mimic the 2-D video analysis used in the PMHS experiments. The total compression was measured as the YZ-plane distance between the impactor and shoulder point. The skeletal compression was measured as YZ-plane distance between the sternum and T6 vertebral process.
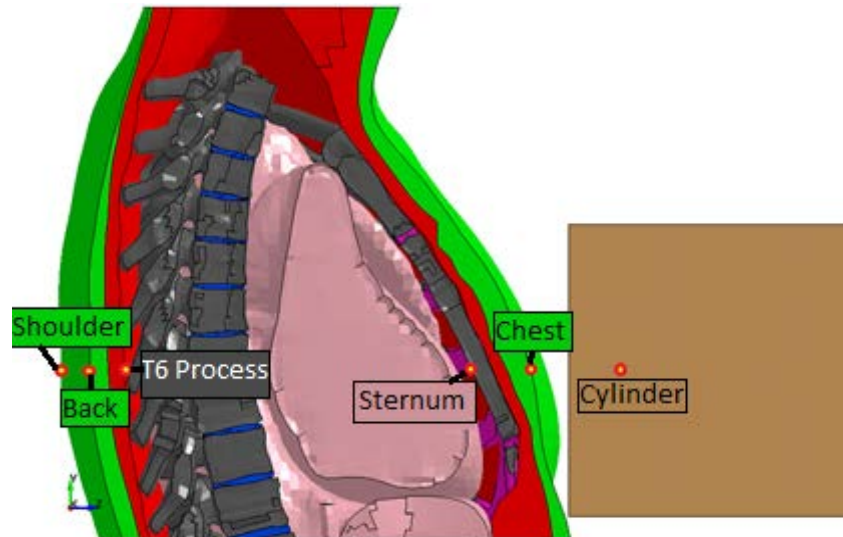
Fig. 4   Sagittal view of measurement points in the ARL torso finite element model from left to right: shoulder, back, sixth thoracic vertebra process, sternum, chest, and impactor. All points except for the shoulder fall along the midline of the body.

The total force exerted by the impactor on the chest was reported by the sliding contact between the impactor and the skin in the RcForc file. Directional components (X, Y, Z axes) and magnitudes were recorded. Z-axis force-time data were collected and filtered with an SAE 600-Hz filter before comparison against the PMHS experiments. The Z-axis force data were also cross-plotted with the total compression and skeletal compression data to create force-displacement curves similar to the ones published by Kroell et al. (1994).

Energy absorption was measured by integrating the force-total displacement curve using a trapezoidal integration scheme. Curves were divided into a loading and unloading phase, with the loading phase including the portion of the curve up to

and including the peak compression. The unloading phase included the portion after peak compression. For the curves that did not complete a full cycle, a linear extension from the final data point to the origin was added to close the loop. Percent energy absorption was calculated as $1 - E_{unload}/E_{load}$.

The global energies and internal energies by parts were collected from the GlStat and MatSum files. Global total energy was evaluated for agreement with the impactor initial kinetic energy (529 J) and conservation of total energy through the simulation. The total energy distribution between kinetic, internal, and contact energy at peak total compression was also analyzed. Total internal energy data from MatSum were broken down into 5 groups (ligaments, bones, cartilages and vertebral discs, flesh and skin, and internal organs) to identify where energy was being absorbed and which materials to prioritize for future efforts.

2.3 Simulations

Sixteen simulations were planned for this study: the original ARL torso simulation and an additional 15 simulations. These additional simulations were broken up into 3 different groups. The first group was themed around modifications to one single material class to isolate the contribution of each class to the overall chest response. The second group combined multiple alterations from the first group into single simulations in an attempt to match the chest compressions observed in the PMHS experiments. The final group consisted of simulations in which the torso mesh was altered by adding the cortical rib shells or additional body weight. Each alteration will be described in detail in the following sections. The full list of themed groups with their assigned simulation names and brief descriptions is as follows:

- Original simulation

- Single material modification:

    o Empty: Deleted all organs

    o Ribs: Lowered moduli of homogenized bone

    o Foam: Organ material switched to low density foam

    o Foam2: Organ material switched to stiffened low density foam

    o NLV: Organ material switched to nonlinear viscous solid

    o NLV2: Organ material switched to stiffened nonlinear viscous solid

    o Ogden: Organ material switched to viscous Ogden rubber

    o Flesh: Flesh material switched to nonlinear viscohyperelastic rubber

- Multiple material modifications:

    o ComboF: Combined Foam2 and Flesh simulations

    o ComboN: Combined NLV2 and Flesh simulations

    o ComboO: Combined Ogden and Flesh simulations

    o All: Combined Ribs, Foam2, and Flesh simulations

- Mesh modifications:

    o RibShellsAll: Split ribs in All simulation into layers

    o WeightAll: Added additional body weight to All simulation

    o WeightEmpty: Deleted all organs from WeightAll simulation

All simulations were run on the High Performance Computing Center Excalibur cluster using the LS-DYNA 9.0.1 FE solver (LSTC 2016). The LS-DYNA software was selected for its broad usage in both government and academia. Each simulation computed a maximum of 50-ms simulated time to ensure capture of the full impact event. The ARL torso FE model can be used with other FE software (ParaDyn, Sierra, and ALE3D) as well.

2.4 Comparison of Simulations and Experiments

In this study, the results from the ARL torso FE model were evaluated primarily by comparison with the results from the 2 experimental PMHS tests. The parameters of interest for this study are as follows:

- Peak impactor Z-force

- Maximum total compression

- Shape of force-deflection curve

- Energy absorbed by force-deflection loop

The shape of the force-deflection curve was a qualitative metric that ideally should reproduce certain key features. Refer to Fig. 1 for examples. The loading phase of the curve should be bilinear with a quick ramp up to near peak force with minimal compression followed by a relatively constant force as the compression increased to peak value. The unloading phase should quickly unload the torso to near-zero force prior to the chest beginning to return to its original depth. The large separation between the loading and unloading curves allowed for the majority of impact energy to be absorbed.

3. Results

3.1 Original

The results from the unmodified torso model were very stiff and chest compressions were low (Fig. 5). The 29.9-kN (6,730-lb$_f$) peak force was much higher than expected. Maximum skeletal compression was 13.3 mm (0.52 inches) and maximum total compression was 20.5 mm (0.81 inches). Both peaks occurred at 4.1 ms. After impact there was a small rebound (3.6 mm) in the skeletal compression. The negative trend in total compression occurred because the impactor was 1 of the 2 measurement points and could separate from the torso. After the impact, the impactor continued to slowly advance at –0.88 m/s while the torso was accelerated to –4.88 m/s.
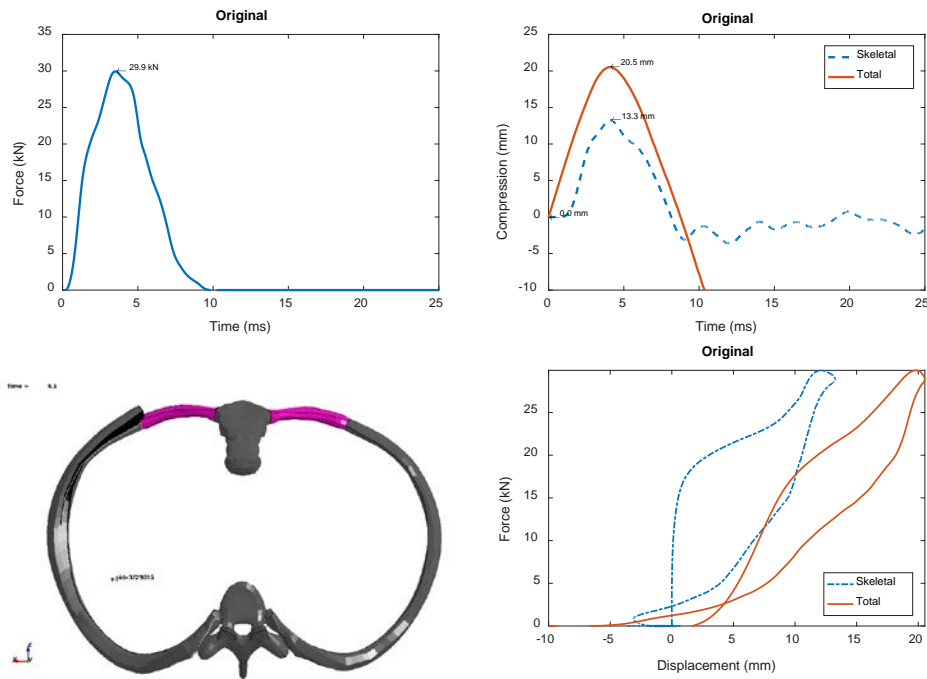
Fig. 5 Original simulation results: force-time (upper left), compression-time (upper right), trace of fifth rib to maximum compression (bottom left); force-displacement (bottom right)

The force-deflection curve absorbed 33.2% of the impact energy, which was low. The bilinear and force-limited behavior was also missing. Total global energy remained consistent at 529 J throughout the entire simulation, but there was a substantial amount of negative sliding energy. No initial penetrations were reported in the simulation initialization, so the negative energy might have been caused by edge detection challenges with sliding contacts. At 4.1 ms, the total energy breakdown was 58.3% kinetic, 60.8% internal, and –19.0% sliding energies. There was no measurable hourglass or external energies in this or any subsequent simulation.

Figure 6 shows the chest response in 5-ms intervals. The lack of compression was particularly visible in the side view, which shows the entire chest undergoing a rigid body-like rotation rather than compressing the ribs and chest cavity. This rotation increased the skeletal compression and decreased the total compression measurements. The impactor slowed from –6.71 m/s to –0.88 m/s after impact, at which time the torso was also moving at roughly –4.88 m/s along the Z axis.

| 5 ms | 10 ms | 15 ms | 20 ms | 25 ms |
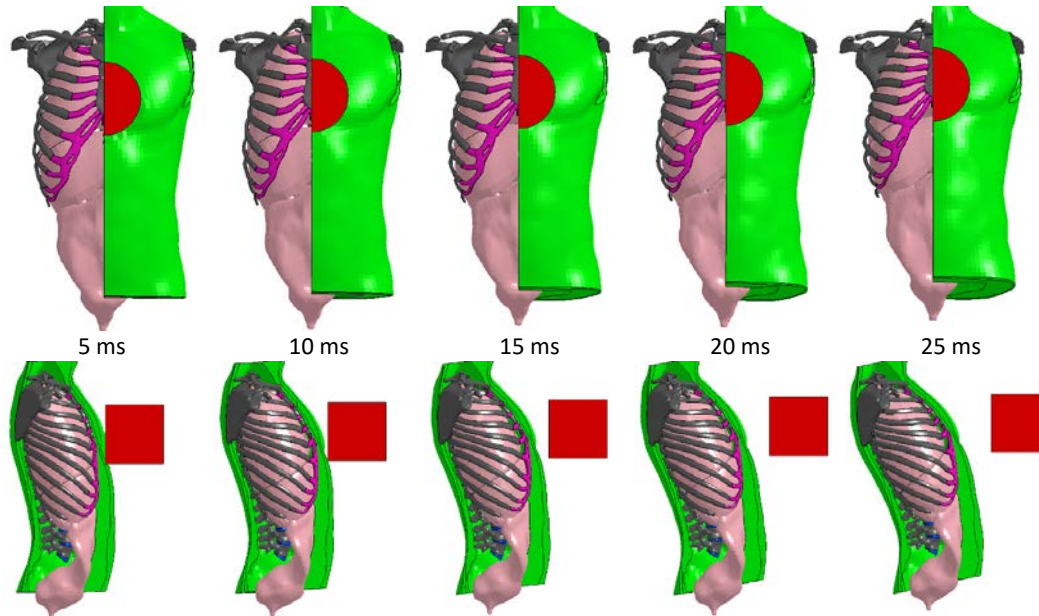
Fig. 6   Original simulation chest response as seen from front (top) and side (bottom). Half of the flesh, skin, and impactor have been hidden to show the bone and organ response.

3.2 Empty

A new simulation, called Empty, was created by removing all internal organs and the ligaments connected to an internal organ. It was hypothesized that the internal organs, which were modeled with a linear elastic material, were too stiff relative to in-vivo organs. This resulted in unrealistically low chest compression and high peak force. This modification reduced the torso weight by 9.5 kg, a 30.8% drop in the total mass.

Figure 7 shows that the removal of the organs and associated ligaments reduced the chest stiffness. However, the response was still stiffer than desired. Peak force fell 53.5% from 29.9 kN to 13.9 kN (3,135 lb$_f$). Maximum total compression increased to 29.9 mm (1.20 inches) at 6.2 ms, a 45.9% increase. Maximum skeletal compression also increased to 30.5 mm (1.29 inches) at 6.7 ms. The skeletal and total compressions were nearly identical. The difference between these measures is the combined compression of the soft tissues at the front and back of the chest. The

ribs and soft tissues were characterized by a material so stiff that no compression occurred. Instead, the chest walls flexed similar to a tube being flattened under a lateral load. Large oscillations in the skeletal compression occurred post-impact because the remaining body parts were still using elastic material characterizations, which could not dissipate the stored impact energy.
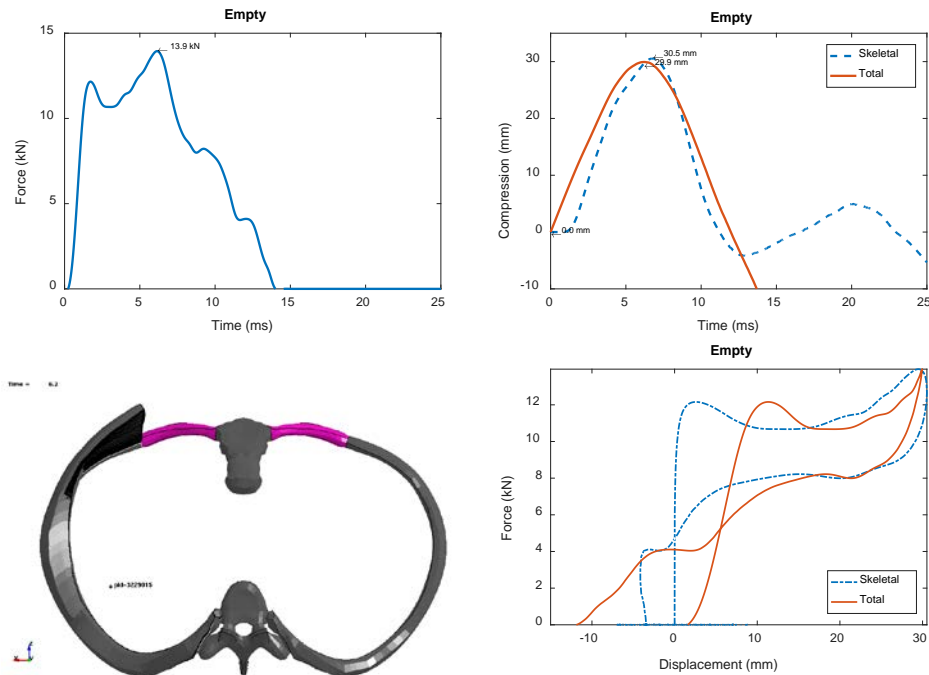
Fig. 7   Empty simulation results: force-time (upper left), compression-time (upper right), trace of fifth rib to maximum compression (bottom left), force-displacement (bottom right)

The loading phase of the force-displacement curve gained a force-limiting response and a clearly defined bilinear behavior. The impactor force in the unloading phase was unrealistically high and more linear in behavior. The elastic response of the chest allowed contact force to be sustained even as the chest expanded beyond its initial depth by 7.0 mm (0.28 inches). The narrowness of the full loop and the crossing of the loading and unloading curves resulted in minimal energy absorption (9.6%).

Energy balances were stable with 529 J of total energy. The energy distribution at the time of peak compression was 63.8% kinetic, 34.3% internal, and 1.9% sliding energies. This simulation had a positive sliding energy, which suggested that the negative sliding energy in the Original simulation was caused by difficulties in resolving the surfaces of the organ-organ and organ-bone contacts. After impact, the impactor and torso were moving –1.78 m/s and –6.21 m/s in the Z-axis, respectively. Both speeds were higher than observed in the Original simulation and skewed the energy distribution toward kinetic energy.

3.3 Ribs

All of the bones in the torso model, including the ribs, were modeled as a single type of homogenous bone with material properties in between those of cortical and trabecular bone. Since the real ribs comprise thin cortical shells with variable thickness over a trabecular core, it was hypothesized that the bone response was too stiff. The elastic moduli for the ribs, scapulae, and clavicles were lowered from 1500 to 400 MPa. The densities and Poisson's ratios were not changed. The properties of the vertebrae and sternum were not changed.

Figure 8 shows the results for the Ribs simulation, which were similar to those of the Original simulation. Reducing the moduli of the ribs slightly increased the peak skeletal compression to a peak value of 13.7 mm (0.54 inches). Peak total compression increased to 20.8 mm (0.82 inches). Both measures reached peak value at 4.1 ms. Total compression increased by 1.5% over the Original simulation despite lowering the moduli by 73%, reinforcing the hypothesis that the organs and soft tissue were too stiff. Peak force fell 2.7% relative to the Original simulation to 29.1 kN (6,543 lb$_f$).
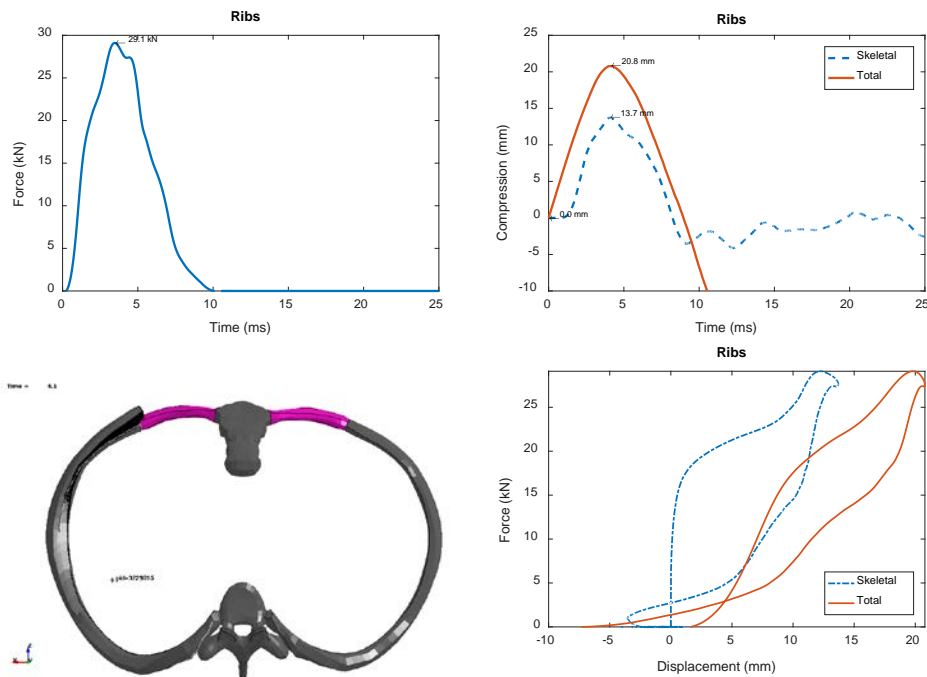
Fig. 8   Ribs simulation results: force-time (upper left), compression-time (upper right), trace of fifth rib to maximum compression (bottom left), force-displacement (bottom right)

The force-deflection response closely resembled the Original simulation. Energy absorption increased slightly to 34.8%. The response was more linear than bilinear and lacked the desired amount of energy absorption. Energy values were consistent

at 529 J although the contact issues leading to negative sliding energy remained. The simulation energy distribution was 58.0% kinetic, 61.9% internal, and –19.9% sliding contact.

3.4 Foam

New material properties based on the LS-DYNA low-density foam (mat57) model were selected in an attempt to reduce the stiffness of the internal organs. These properties, shown in Table 2, were collected from a compendium of numerous characterizations of human and porcine internal organs for development of the Total Human Model for Safety (THUMS) FE model (Shigeta et al. 2009). Unfortunately, this reference specified only the material model and stress-strain response. These material curves were supplemented with values from Rater (2013) (Table 3), which continued development of the THUMS model and provided the missing parameters. Together, a complete material model was formed that could be used in the ARL torso model. The material curve for the liver was also applied to the pancreas, which was not characterized in the referenced data.

Table 2   Nominal stress (kPa)–strain curves for internal organs (Shigeta et al. 2009)

Organ	$\varepsilon = 10\%$	$\varepsilon = 20\%$	$\varepsilon = 30\%$	$\varepsilon = 50\%$
Heart	5.4	12.4	28	374.9
Lung	7.9	14.1	20.1	31.7
Liver	2.5	14.7	58.9	380.2
Spleen	1.5	2.5	3.7	9.8
Kidney	4.9	36.3	134.4	…
Small intestine	17.7	38.2	94.1	778.6
Large intestine	16.3	29.4	40.9	163.4
Blood vessels	14.9	29.7	66.9	193.2
Stomach	4.5	12.7	28.1	93.2

Table 3   Parameters for MAT_LOW_DENSITY_FOAM (Rater 2013)

Parameter	Value	Parameter	Value
ρ	1000 kg/m^3	β	0
E	0.1 MPa	Damping	0.3
Hu	0.1	Shape factor	1

The Foam simulation terminated early at 4.4 ms due to negative volumes in the left lung. An example of the mesh warping preceding the termination is shown in Fig. 9. The negative volume was caused by spalling elements that exceeded the maximum definition in the stress-strain curve.
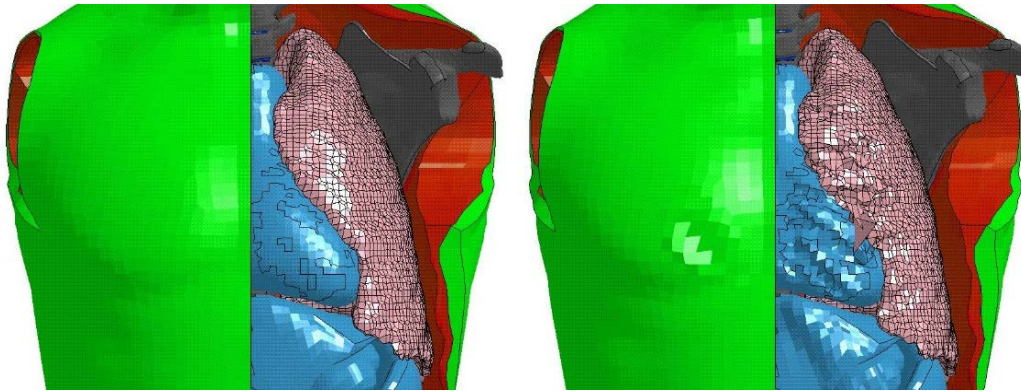
Fig. 9 **Foam simulation: left lung was distorted from original mesh (left) to unstable mesh at 4.4 ms (right) due to localized loading from the left ribs. Left ribs, clavicle, and sternum not shown to improve visibility of organs.**

The results are shown in Fig. 10; the final skeletal deflection was 22.5 mm (0.89 inches) and the final total compression was 26.2 mm (1.03 inches). Neither deflection had reached peak value by the termination time. The final impactor force also did not reach maximum but was 13.2 kN (2,978 lb$_f$) at the simulation end. The loading phase of the force-deflection curve showed the desired bilinear response. The energy absorption could not be calculated because the simulation terminated before unloading.
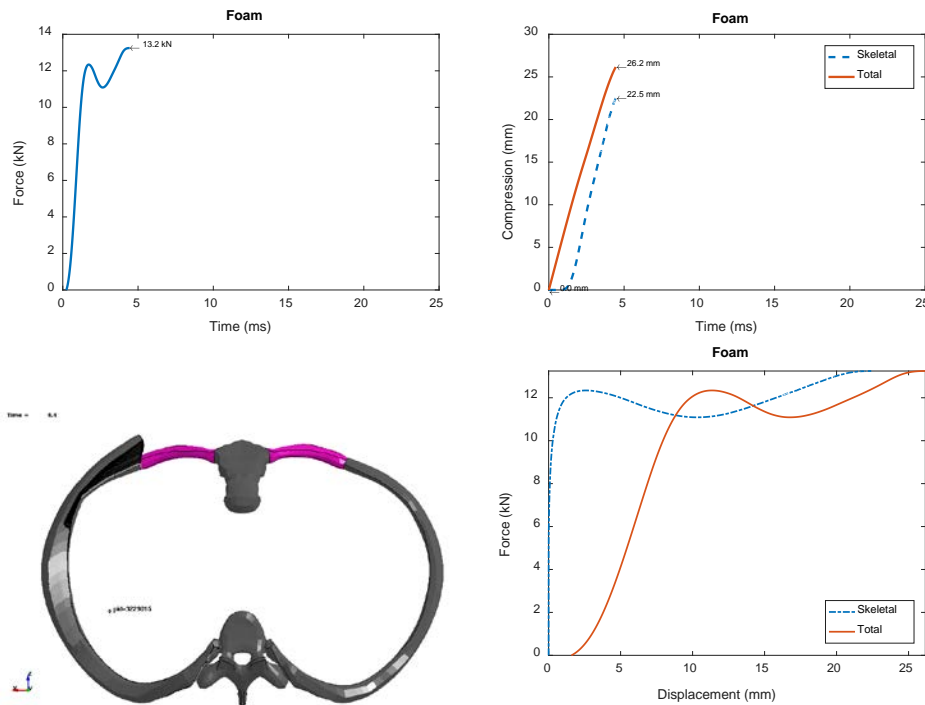

Fig. 10 **Foam simulation results: force-time (upper left), compression-time (upper right), trace of fifth rib to maximum compression (bottom left), force-displacement (bottom right)**

13

3.5 Foam2

This simulation uses the same Mat57 material definitions that were used in the Foam simulation. This time, 2 additional data points (60%, 180 MPa) and (70%, 1800 MPa) were added to the stress-strain curves in Table 2 to stiffen the organs after compressing greater than or equal to 60% to avoid negative volume errors.

The material changes prevented termination due to negative volume but also dropped the default time step by approximately one-fourth. Figure 11 presents the simulation results, which show improved, but still lower than expected, compression. Skeletal compression reached a maximum of 26.0 mm (1.02 inches) at 6.4 ms. Maximum total compression reached 27.8 mm (1.09 inches) at 5.8 ms, an increase of 35.6% compared to the Original simulation. Peak force dropped by 42.8% to 17.1 kN (3,844 lb_f), slightly higher than the peak force of the Empty simulation.

Fig. 11   Foam2 simulation results: force-time (upper left), compression-time (upper right), trace of fifth rib to maximum compression (bottom left), force-displacement (bottom right)

The force-deflection curve displayed a bilinear loading phase with force-limiting behavior. The energy absorption dropped to 29.7% because the softer organs allowed for relatively more flexion than increased compression. The unloading phase was similar to the Empty simulation with relatively linear unloading and sustained force through the post-impact rebound.

Global energy balances were stable at 529 J total energy. At 5.8 ms, the energy distribution was 53.5% kinetic, 43.4% potential, and 3.1% sliding energies. The positive sliding energy was a good indicator of well-behaved contacts and also implied that the contacts between organs were the source of the negative energies in the preceding simulations.

3.6 Nonlinear Viscoelastic (NLV)

The low-density foam model was successful in increasing the chest compression, but it also increased the wall time needed to complete the simulation by 4 times. An alternative nonlinear viscoelastic (NLV) foam material (Mat62) was employed in an attempt to soften the internal organs without reducing the time step. The adapted model is summarized in Table 4. Since the density was omitted from the material description, a density of 1000 kg/m^3 was assumed. This matched the density used in the materials described in the Foam simulation. The missing organs (heart, lungs, intestines, pancreas, and stomach) were assigned the same properties as the liver because it was the softest of the 3 defined organs.

Table 4   Fitted nonlinear viscous foam material parameters (Lee and Yang 2001)

Parameter	Liver	Spleen	Kidney
E1	0.185 MPa	0.488 MPa	0.352 MPa
E2	0.10 MPa	0.25 MPa	0.15 MPa
N1	4	4	10
PR	0.45	0.45	0.45
V2	15.0 N·ms/mm^2	15.0 N·ms/mm^2	15.0 N·ms/mm^2
N2	0.2	0.2	0.2

The NLV simulation avoided the time step reduction seen in the Foam and Foam2 simulations, but error terminated at 3.1 ms due to negative volumes. The negative volumes were caused by excessive deformation in the left lung, similar to the distortion shown in Fig. 9. At termination, the skeletal compression was 13.0 mm (0.51 inches) and total compression was 19.1 mm (0.75 inches). The force reached a local maxima at 12.5 kN (2,810 lb$_f$). The results are shown in Fig. 12. Neither the compressions nor the force appeared to have reached peak values. The force-deflection showed a bilinear and force-limited loading phase, but the simulation terminated before the unloading phase and energy absorption could be determined.
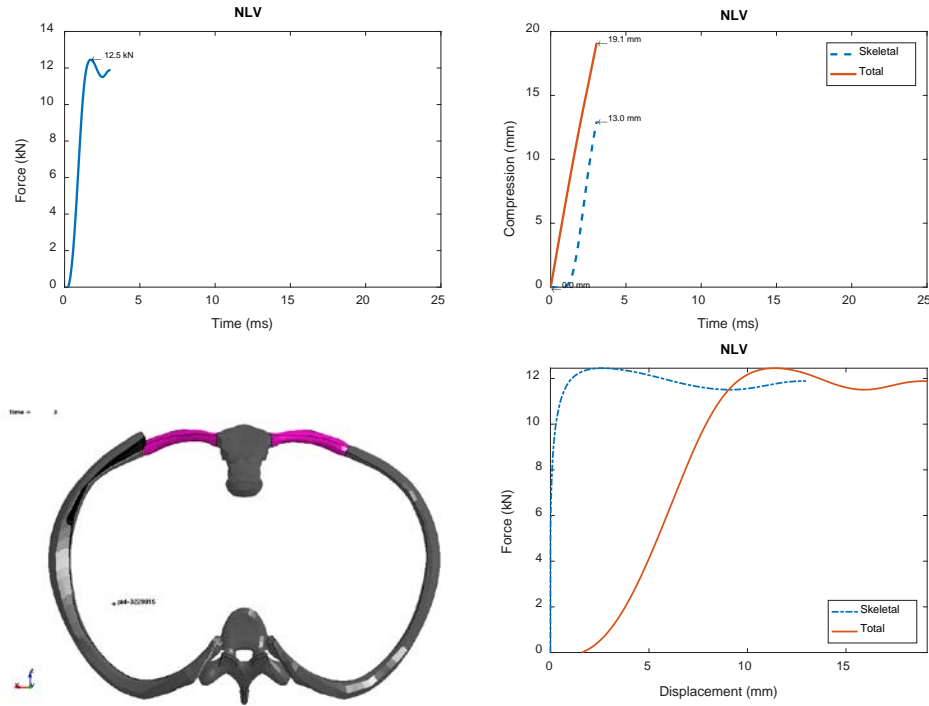
Fig. 12   NLV simulation results: force-time (upper left), compression-time (upper right), trace of fifth rib to maximum compression (bottom left), force-displacement (bottom right)

3.7 Nonlinear Viscoelastic 2 (NLV2)

The NLV material model has a built-in stability mechanism in the term E2, which was an artificial term intended to stiffen the material to prevent element inversion and warping. The material model developed by Lee and Yang (2001) used this term to capture the nonlinear behavior of the organ tissue. The low value of E2 prevented the material model from stiffening in response to extremely large deflections. A new simulation, NLV2, was developed in which the E2 values were multiplied by 1,000 for all internal organs to prevent element erosion and negative volumes.

Figure 13 shows the results for the NLV2 simulation. Changing the values of E2 was successful in improving the simulation stability. The chest response was softer than the Original simulation but slightly stiffer than the NLV simulation. Skeletal compression peaked at 22.1 mm (0.87 inches) at 6.2 ms, whereas the total compression peaked at 25.9 mm (1.02 inches) at 5.4 ms. The total compression was not as high as observed in the Foam2 simulation but was 26.3% higher than the Original simulation. Peak force dropped 32.8% to 20.1 kN (4,517 lb$_f$).

Fig. 13 NLV2 simulation results: force-time (upper left), compression-time (upper right), trace of fifth rib to maximum compression (bottom left), force-displacement (bottom right)

Although the peak compression was lower, the energy absorbed in the force-deflection loop increased to 43.9%. The loading phase lacked the expected force-limiting behavior, which resulted in less pronounced bilinear appearance. The unloading phase returned less energy but still sustained contact with the impactor through the rebound phase. Global energy was stable at 529 J total energy. At peak deflection, the energy breakdown was 53.1% kinetic, 45.3% internal, and 1.6% sliding energies.

3.8 Ogden

Another alternative material model for soft tissues was the Ogden rubber material model. This material also included an optional viscosity component needed to represent organic tissue in the Mat77 material model. Material characterizations from the published literature were drawn for the kidneys (Snedeker et al. 2002), the liver (Untaroiu and Lu 2013), and the lungs (Naini et al. 2011). The material parameters are listed in Table 5. Not all organs were characterized in the referenced studies. The material properties of the lungs were assigned to the heart, stomach, and intestines because these organs contained internal cavities. The material properties from the liver were assigned to the gallbladder, pancreas, and spleen on the basis that all of these organs were solid and vascularized.

Table 5   Fitted Ogden rubber properties for internal organs from literature

Organ	ρ (kg/m³)	PR	N	μ1 (MPa)	α1	μ2	α2	μ3	α3	G1	β1
Lung	600	0.35	0	$4.529 \cdot 10^{-4}$	9.5	…	…	…	…	…	…
Kidney	1000	0.495	0	0.15	0.3	0.526	0.4	−0.01	−9.5	0.93	0.25
Liver	1051	0.495	0	$6.06 \cdot 10^{-3}$	7.46	…	…	…	…	…	…

The Ogden simulation terminated early due to negative volumes and energy growth at 7.7 ms. Extreme mesh distortion leading to element inversion was caused by the sliding contact between the liver and intestines as illustrated in Fig. 14. The simulation did run long enough to capture the full loading phase. The simulation time step was unchanged, but there was a 15% reduction in the simulation progress rate relative to the Original simulation.
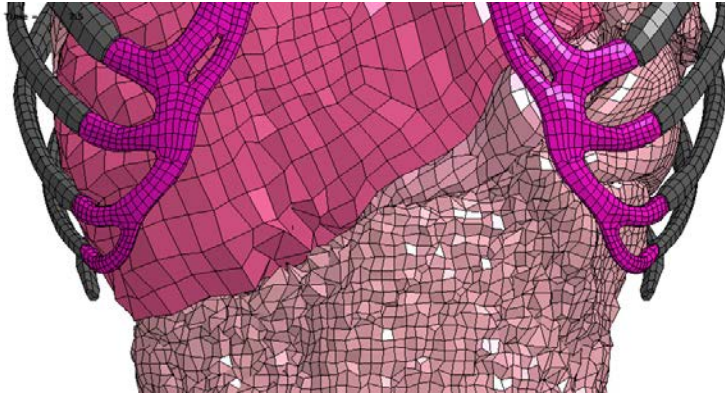
Fig. 14   Ogden simulation: mesh distortion at the sliding contact between the liver and intestines prior to termination

The Ogden material model was softer than the Foam2 and NLV2 material models. The results are shown in Fig. 15. The peak skeletal compression was 29.7 mm (1.17 inches) at 6.6 ms. Total compression peaked at 6.1 ms at 29.6 mm (1.17 inches), 44.4% higher than the Original simulation. Peak force was 15.4 kN (3,462 lb$_f$). Both the skeletal and total compression were nearly identical, a trait observed previously in the Empty simulation and attributed to flexion-dominated response.
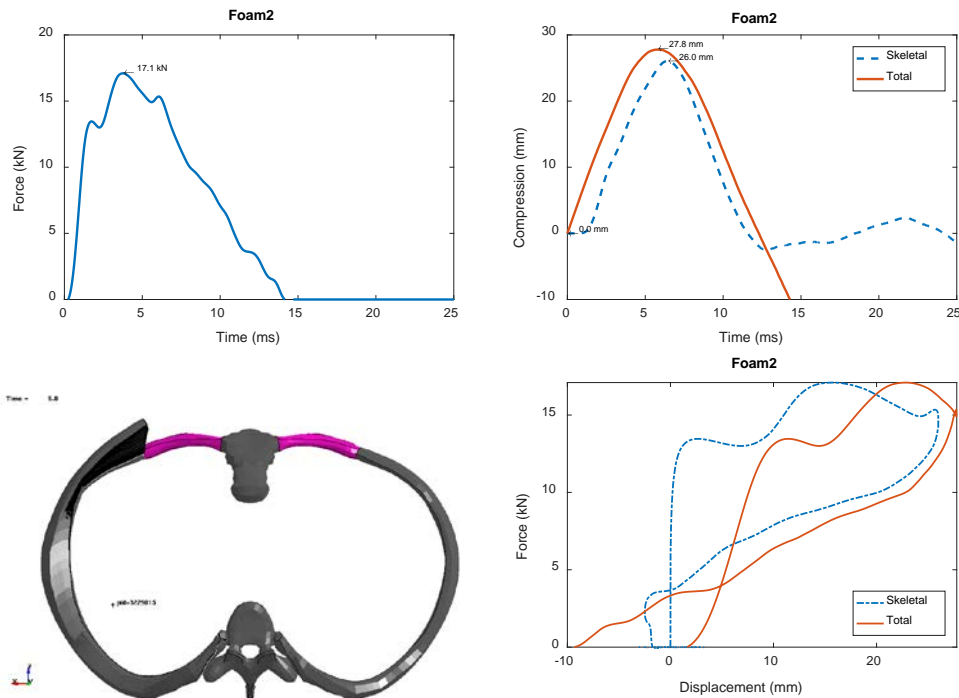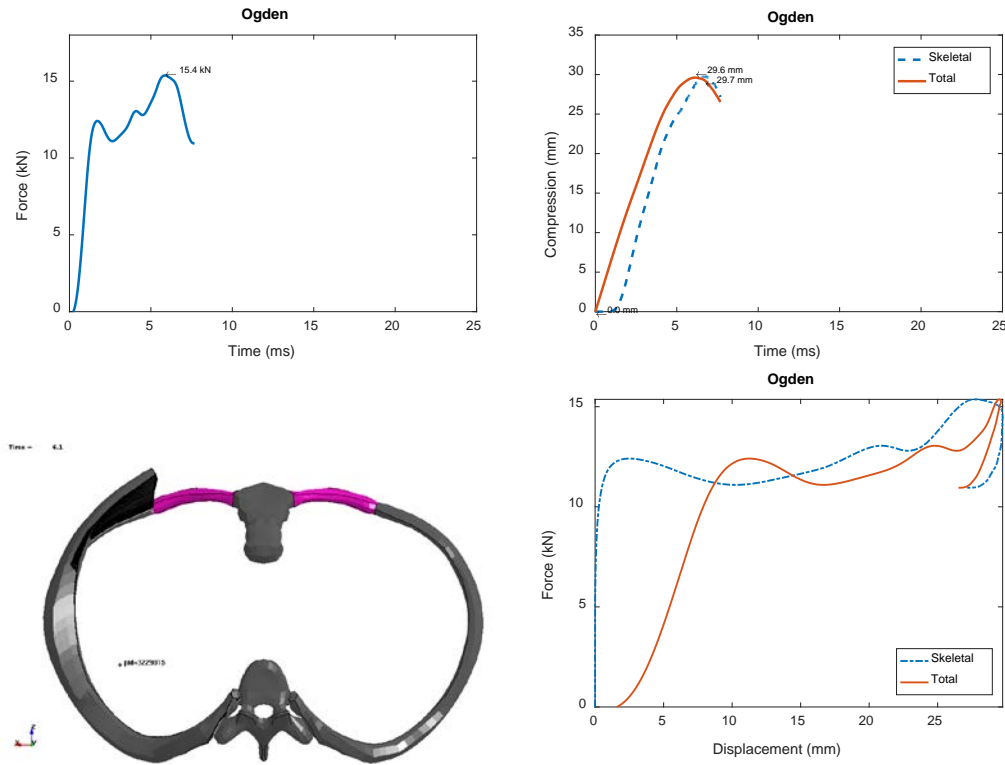
Fig. 15 **Ogden simulation results: force-time (upper left), compression-time (upper right), trace of fifth rib to maximum compression (bottom left), force-displacement (bottom right)**

The loading portion of the force-deflection curve captured the expected bilinear and force-limiting behavior. Only a small portion of the unloading curve was captured, but the curve as a whole closely resembled the force-deflection curve of the Empty simulation. Total energy remained stable at 529 J until termination with 63.2% kinetic, 41.3% internal, and –4.5% sliding energies at the time of peak compression.

3.9 Flesh

Softening the internal organs increased the chest compression, but the compression was still lower than expected. A new simulation path was pursued: returning to the Original simulation and changing the material properties of the flesh to a hyperelastic, viscoelastic material model (mat92). This material model was used in the tetrahedral leg model (Hampton and Kleinberger 2017), which added additional fiber characterization to the material model from a previous lower leg injury study (Dong et al. 2013). The skin, which consisted of all elements on the outermost surface layer, was left unchanged as a linear elastic material to avoid altering the contact behavior with the impactor. The material parameters are summarized in Table 6.

Table 6   Flesh material parameters for Mat92

Property	Value	Property	Value
ρ	1300 kg/m^3	C1	120 Pa
XK	20 MPa	C2	250 Pa
XLAM	5	C3	1 MPa
XLAM0	1	C4	1.2
FAILSF/FAILSM	0	C5	100
S1	1.2	T1	23 ms
S2	0.8	T2	63 ms

The Flesh simulation terminated at 22.3 ms due to warped elements in the neck flesh causing negative volume errors. Figure 16 shows the original and distorted mesh. The mesh distortion was localized to the free edges at the end of the mesh where there was minimal constraint on nodal motions. Fortunately, the simulation made sufficient progress to analyze the full chest response.
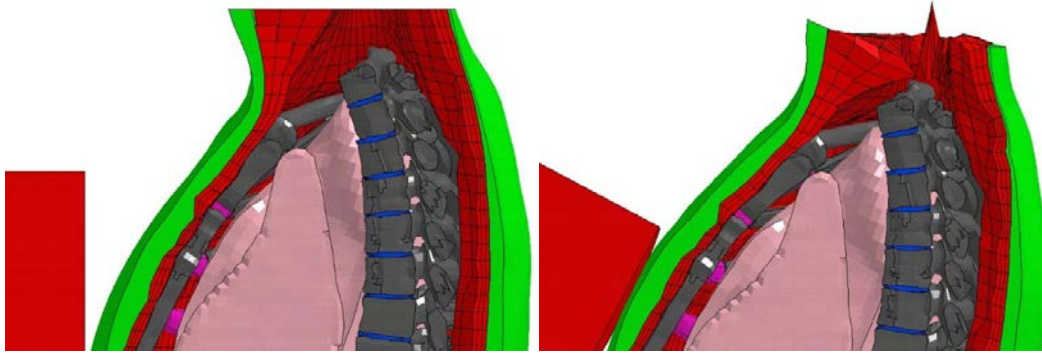
Fig. 16   A sagittal plane view through the midline of the torso in the Flesh simulation. The soft tissue mesh in the upper neck was highly distorted at 21.2 ms (right) compared to the original mesh (left).

Figure 17 shows the simulation results. The peak skeletal compression was 12.4 mm (0.49 inches) and occurred at 6.1 ms. Peak total compression was 35.4 mm (1.39 inches) at 7.3 ms, 72.7% higher than the Original simulation. The difference between the 2 peak compressions was 23 mm (0.91 inches). The skeletal compression was actually lower than the Original simulation because of the increased protection from the flesh. The softer tissue mitigated the impact force to 19.8 kN (4,462 lb$_f$), a similar reduction to the Foam2 and NLV2 simulations.
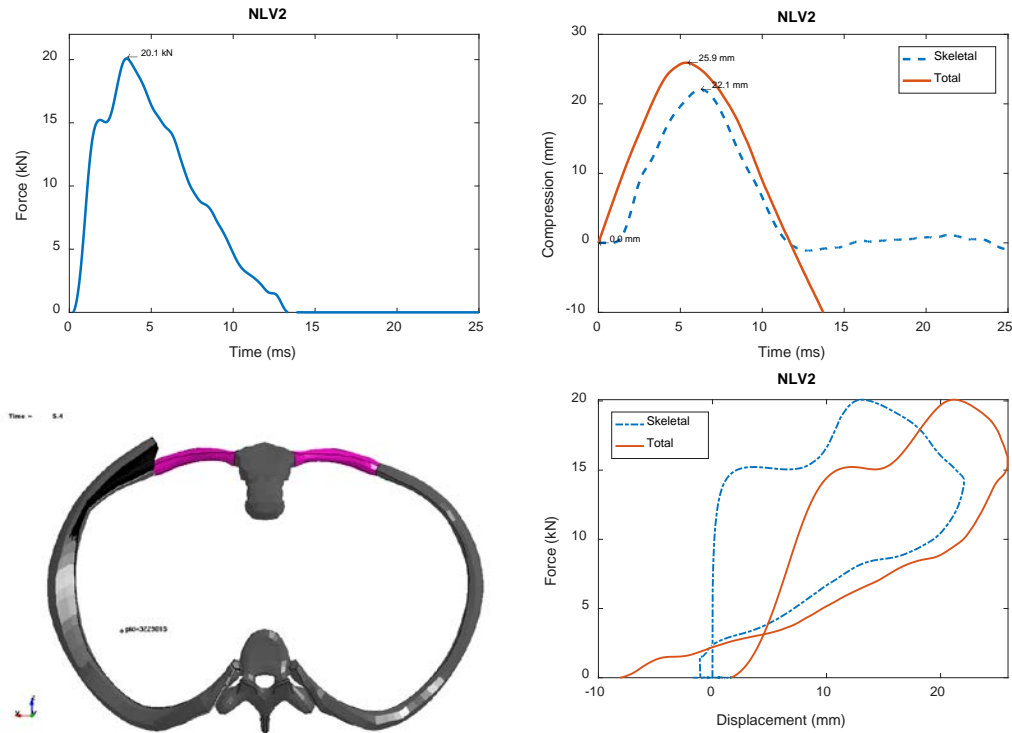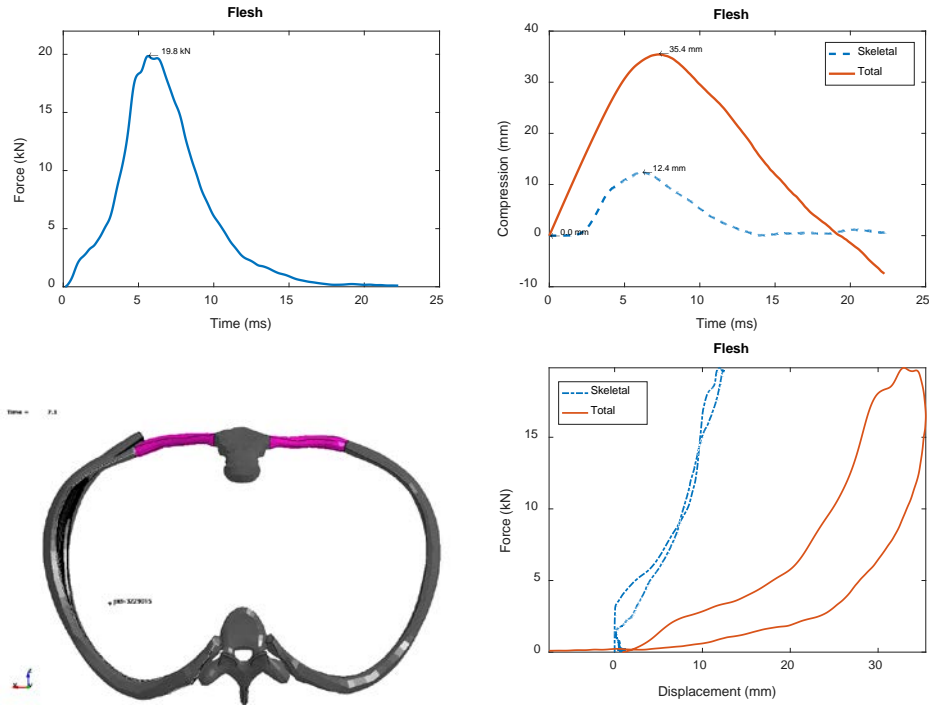
Fig. 17 Flesh simulation results: force-time (upper left), compression-time (upper right), trace of fifth rib to maximum compression (bottom left), force-displacement (bottom right)

The force-deflection loading phase behaved more like an exponential growth function as opposed to the expected bilinear, force-limited curve. This behavior came from the exponential characterization of the collagen fibers in the soft tissue. Despite the difference in shape, the total absorption was 60.9% of the impact energy. Unlike previous simulations, the skeletal force-deflection showed a different, linear elastic-like behavior with minimal energy absorption. The soft tissue changes were not able to reproduce the force-limiting behavior but were able to capture a bilinear unloading behavior.

Global energy balances were stable at 529 J until just prior to termination, after which the total, potential, and kinetic energies started to grow exponentially. Energy distribution at 7.3 ms, the time of peak compression, was broken down into 60.9% kinetic, 42.0% internal, and –2.9% sliding energies. The sliding contact issues leading to negative energy were minimized since less of the impact load was carried by the internal organs. The energy growth in flesh elements in the right side of the neck were contributors to the early termination.

3.10 ComboF

Modifying single subcomponents in the FE models yielded small improvements in the chest compression and the force-compression response. The first simulation in

the multiple modifications group, the ComboF simulation, was developed in an attempt to combine the loading phase improvements from the Foam2 simulation with the lowered force and improved unloading phase behavior from the Flesh simulation.

The ComboF simulation was more stable than the Flesh simulation, albeit slow due to the reduced time step inherited from the Foam2 simulation. The simulation terminated at 30.6 ms due to a sudden contact failure between the sternum and sixth costal cartilages. Figure 18 shows that the combination of 2 softening techniques was very effective at increasing the chest compression. Skeletal compression peaked at 40.3 mm (1.59 inches) at 18.3 ms and total compression peaked at 61.0 mm (2.40 inches) at 14.3 ms. The total compression was 197.6% higher than the Original simulation, but still fell short of the experimentally observed compression. Peak force dropped further to only 7.0 kN (1,567 lb$_f$).
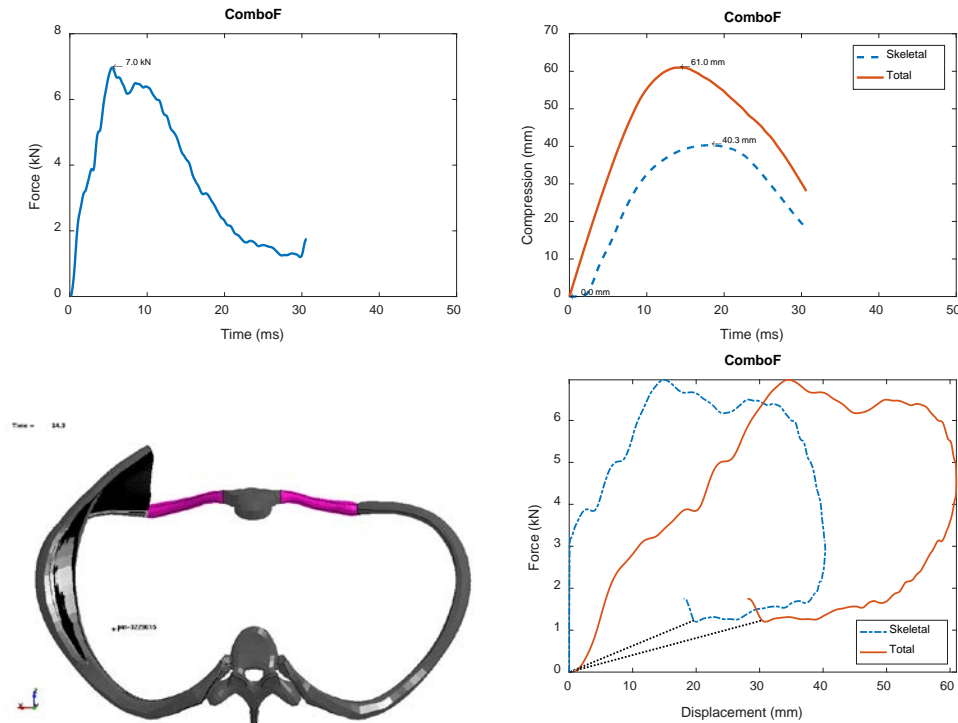
Fig. 18   ComboF simulation results: force-time (upper left), compression-time (upper right), trace of fifth rib to maximum compression (bottom left), force-displacement (bottom right)

The loading phase of the force-deflection curve showed the desired bilinear shape and force-limiting behavior. The unloading phase also showed a bilinear response with a rapid drop in force prior to the compression receding. The energy absorption improved to 74.8%, the highest yet despite a small amount of force remaining in the post-impact phase. The sudden force increase on the curve tail was an artifact of the early termination and was removed prior to calculating the energy absorption.

Global total energy was stable at 529 J up to just prior to termination, with the energy at peak compression distributed between 53.5% kinetic, 45.2% internal, and 1.2% sliding energies.

3.11 ComboN

Combining multiple alterations in the ComboF simulation succeeded in softening the chest response while improving upon the element stability compared to the Flesh simulation. An alternative simulation, ComboN, was developed by combining alterations from the NLV2 and Flesh simulation in an attempt to keep the improved chest response without the time step drop from the Foam2 material model.

The ComboN simulation was mostly stable until negative volume termination at 31.4 ms, after sliding contact between the intestines and liver broke down, similar to the Ogden simulation. The torso sustained a maximum skeletal compression of 25.9 mm (1.02 inches) at 14.6 ms as shown in Fig. 19. Maximum total compression was 49.5 mm (1.95 inches) at 12.1 ms. While this was 141.5% higher than the Original simulation, it was not as soft as the ComboF simulation response. The peak force of 9.9 kN (2,229 lb$_f$) reflected the higher chest stiffness relative to ComboF.

Fig. 19   ComboN simulation results: force-time (upper left), compression-time (upper right), trace of fifth rib to maximum compression (bottom left), force-displacement (bottom right)

The force-deflection curve showed bilinear loading but lacked force-limiting behavior. The unloading phase behaved as desired although the force elevation prior to termination was present. This force increase was removed prior to calculating the loop energy. Energy absorption edged up to 79.2% due to higher loading and lower unloading forces.

Energy balance was very similar to ComboF, with 529 J total energy distributed over 53.3% kinetic energy, 45.5% internal energy, and 1.2% sliding energy. Total energy was well conserved up until just prior to termination.

3.12 ComboO

A new simulation, ComboO, was created by combining the alterations from the Ogden and Flesh simulations. It was hoped that the increased load sharing by softening both parts in tandem would preserve the large chest compressions from the Ogden simulation while avoiding the early termination.

The ComboO chest response is shown in Fig. 20. The simulation terminated at 8.4 ms due to negative volume in the left lung elements compressed by the fourth rib. While this was longer than the Ogden simulation, the softer chest response increased the impact duration, and the simulation did not progress far enough to reach peak compression. At the end of the simulation, the skeletal compression was 34.5 mm (0.88 inches) and total compression was 52.6 mm (2.07 inches), neither of which had begun to level off. The force peaked slightly prior to termination at 4.2 kN (948 lb$_f$), but it was unclear whether this was the true peak value.

Only the loading phase of the force-deflection curve was present. It showed a bilinear response but did not completely limit the force in the later loading phase. The energy absorption could not be calculated without the unloading phase.

The simulation global energy was stable at 529 J until just prior to termination. At this time, the sliding contact energy went negative and started to grow exponentially. This energy growth, in combination with the relatively choppy appearance of the force-time curve, may indicate difficulties in resolving contact surfaces between the lungs and ribs.
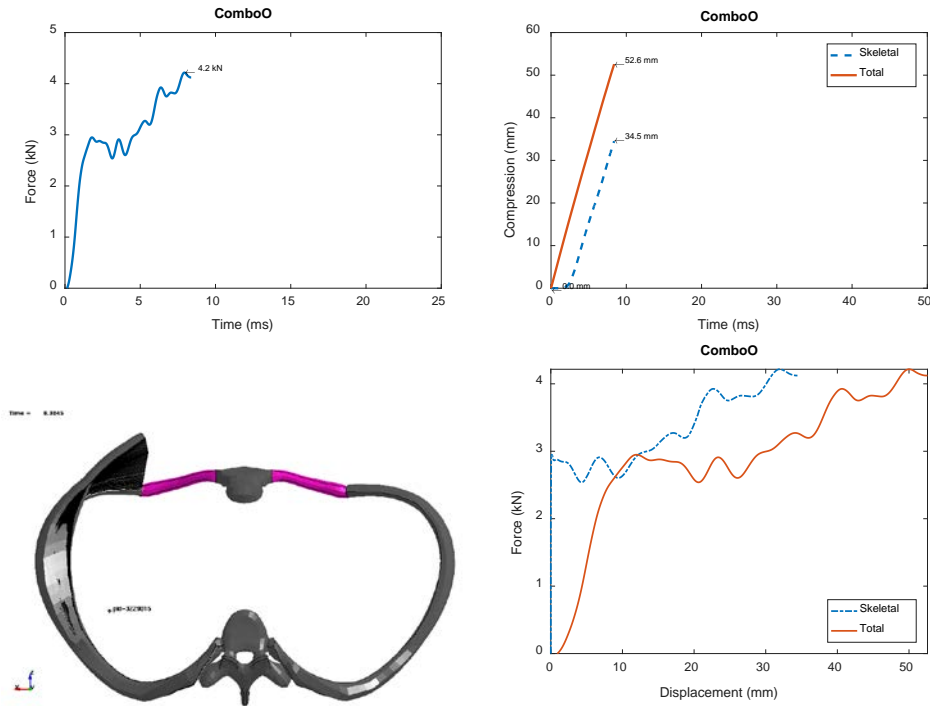
Fig. 20   ComboO simulation results: force-time (upper left), compression-time (upper right), trace of fifth rib to maximum compression (bottom left), force-displacement (bottom right)

3.13 All

The alterations from the Ribs simulation was combined with the ComboF (Foam2 and Flesh) simulation as the All simulation in an attempt to further increase the chest compression. The ComboF simulation alterations were selected over the ComboN simulation for the higher compression and lower force despite the lowered time step.

The results are shown in Fig. 21. The simulation terminated at 30.0 ms due to warped elements in the interior flesh wall in front of the liver (see Fig. 22). The All simulation produced an additional 2.8 mm (0.11 inches) of compression over the ComboF simulation, increasing the peak total compression to 63.8 mm (2.51 inches) at 15.4 ms. The peak skeletal compression was 43.6 mm (1.71 inches) at 20.5 ms. Force peaked at 6.8 kN (1,520 lb$_f$), earlier than either of the compressions.

Fig. 21   All simulation results: force-time (upper left), compression-time (upper right), trace of fifth rib to maximum compression (bottom left), force-displacement (bottom right)

Fig. 22   All simulation: sagittal plane view of the warped flesh elements from a behind-left oblique viewpoint. The liver, gallbladder, and intestines have been hidden to show the interior flesh surface.

The force-deflection curve was bilinear and force-limited in the loading phase. The unloading phase was incomplete due to the early termination and showed the sudden force increase typical of early terminations. This force increase was removed prior to calculating the energy absorption. The closed force-deflection loop absorbed 79.2% of the impact energy.

Much like the ComboF simulation, the All simulation conserved the total energy of 529 J until just prior to termination. Energy distribution was 53.7% kinetic, 45.6% internal, and 0.8% sliding energies.

3.14 RibShellsAll

The first simulation of the mesh modification group, RibShellsAll, was created to address the assumption of homogeneity. Ribs in the human body comprise a relatively soft trabecular core coated in a thin layer of stronger, denser cortical bone. In vivo, the ribs exhibit significant inhomogeneity in shape and strength both along the length of each rib and between ribs (Cormier et al. 2005). In the previous ARL torso FE simulations, the ribs were modeled as homogenized bone with properties that fell in between those of cortical and trabecular bone.

The solid elements making up the ribs in the FE model were covered with a layer of shell elements to better approximate the cortical shell and trabecular core of ribs. The shell layer was given a uniform thickness of 1 mm. The solid elements of the ribs were assigned material properties for trabecular bone while the new shell elements were assigned material properties for cortical bone. The material models are shown in Table 7 and were drawn from Lynch et al. (2015).

Table 7   Material properties for shell-lined solid ribs

Material	Density (kg/m^3)	Modulus (MPa)	Poisson's ratio
Trabecular rib bone	1400	40	0.42
Cortical rib bone	1800	17,000	0.30

The RibShellsAll simulation terminated early at 21.2 ms due to flesh elements warping under contact between the impactor, sternum, and right sixth costal cartilage. The torso compression, shown in Fig. 23, was lower than desired and lower than the All simulation. Total compression was 50.7 mm (2.00 inches) peaking at 12.0 ms. The skeletal compression was 34.7 mm (1.37 inches), which reached peak value at 13.1 ms. The impactor force peaked at 8.4 kN (1,895 lb$_f$).
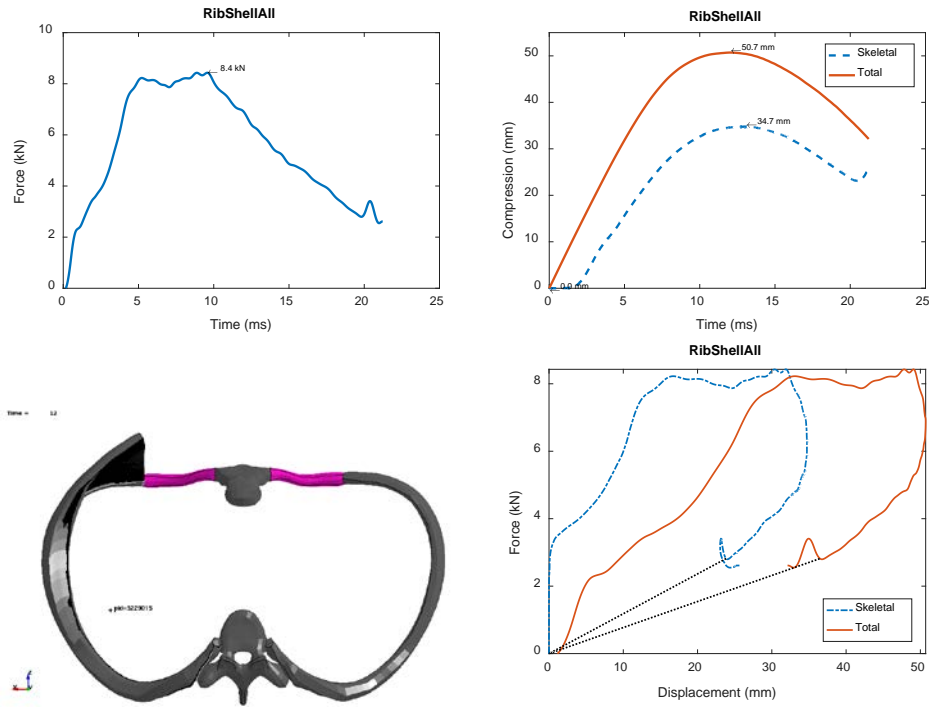
Fig. 23 RibShellsAll simulation results: force-time (upper left), compression-time (upper right), trace of fifth rib to maximum compression (bottom left), force-displacement (bottom right)
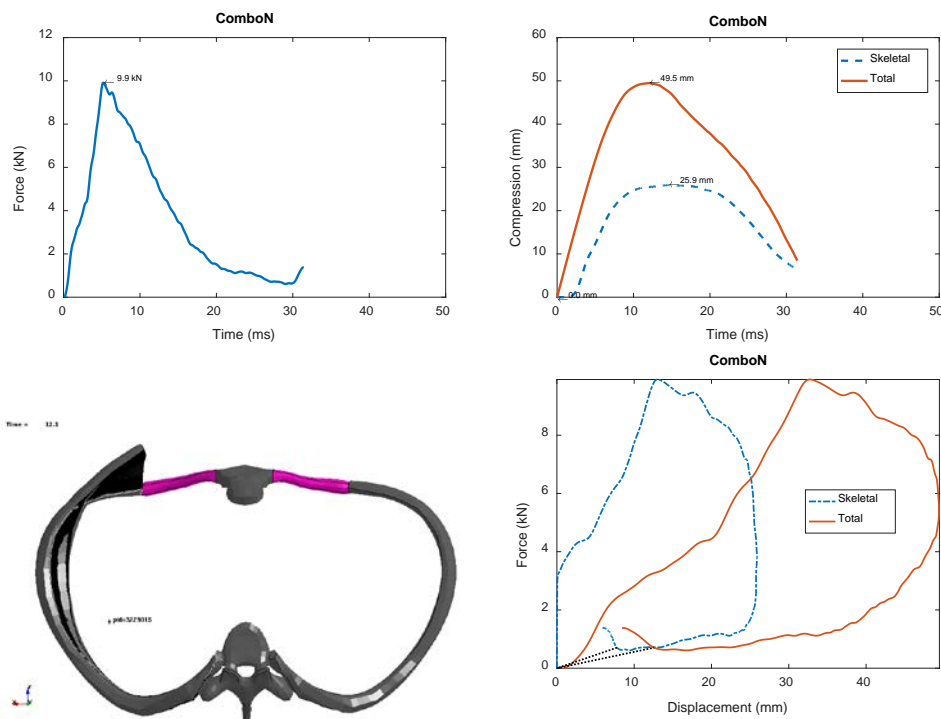
The force-deflection curve showed ideal loading behavior (bilinear and force-limited), but the unloading phase showed that the chest compression started receding before the impactor force was lowered. There was a sudden increase in force at the end of the simulation that was removed prior to calculating absorption. The higher energy return in the unloading phase dropped the absorption to only 61.7%.

The total energy was 526 J distributed as 52.8% kinetic, 46.8% internal, and 0.5% sliding energy. The energies were stable up until termination.

3.15 WeightAll

The second simulation of the mesh modification group was the WeightAll simulation. The PMHS experiments referenced in the Methods section use full body PMHS. However, the ARL Torso FE model included only the torso and upper abdominal parts, resulting in different mass and inertial properties. Point masses were added to the simulation to restore the proper weight and determine how this difference affected the simulation results.

The total weight of the ARL torso model was 30.7 kg (67.7 lb). The expected whole body weight as reported by Zygote Media Group Inc. (2015) was 79.37 kg (175.0

lb), leaving 48.6 kg (107.3 lb) in the unmeshed head, arms, lower abdomen, and legs. Clauser et al. (1969) reported the total body and body segment weights of several medical cadavers, including one weighing 75.1 kg (165.6 lb). These body segment weights were scaled using the ratio of Zygote to Clauser whole body weights and used to calculate the weight of each missing body segment that would need to be added to the FE model (Table 8).

Table 8   Missing weights for unmeshed body regions of the Torso finite element model

Body region	% of total body weight (Clauser et al. 1969)	Weight to be added to finite element model
Head	7.1%	5.65 kg (12.4 lb)
Arm	6.5%	5.15 kg (11.4 lb)
Missing parts of abdomen	9.3%	7.36 kg (16.2 lb)
Leg	16.0%	12.64 kg (27.9 lb)

The missing weights were added to the FE model as point masses, bringing the total weight up to 79.3 kg (174.8 lb). Half of the missing abdomen weight was incorporated into each of the legs. The point masses for the arms and legs were positioned forward of the torso relative to the shoulder and hip joints, respectively, while the head point mass was positioned vertically above the neck. The point masses were then connected to the torso by adding multiple ligaments to improve loading distribution as shown in Fig. 24. The stiffness of these new ligaments was raised to 18,000 MPa to compensate for the small cross-sectional area and minimize the stretch under loading. There were 23 ligaments connecting the head mass to the T1 vertebra and flesh, 14 ligaments connecting each arm mass to the scapula and flesh, and 16 ligaments connecting each abdomen and leg mass to the L5 vertebra and hip flesh.
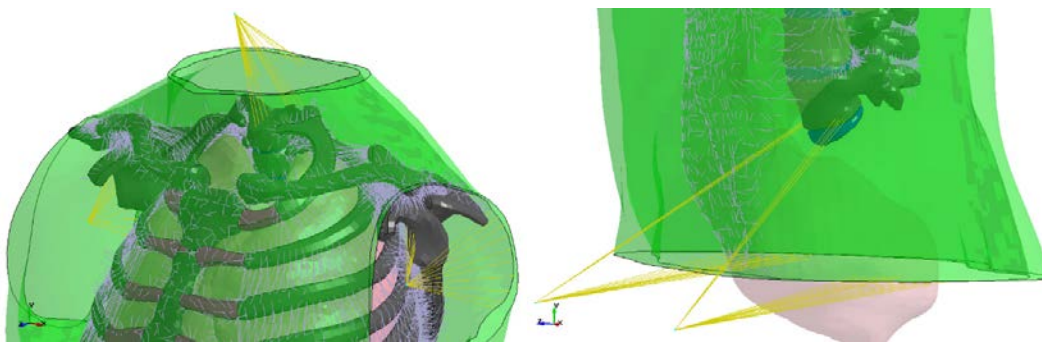
Fig. 24   Stiffened ligaments, shown as orange lines, connect the point masses representing unmeshed head and arms to the neck and shoulders (left) and the lower abdomen and legs to the flesh and vertebrae above the hips (right)

Figure 25 shows the results for the WeightAll simulation. The simulation terminated early at 29.8 ms due to warped elements in the flesh near the sixth right costal cartilage and liver. The skeletal compression reached a maximum of 49.4 mm (1.95 inches) at termination. The total compression also increased to a peak value of 70.6 mm (2.78 inches) at 25.7 ms, a 10.7% increase over the All simulation. Force peaked early at 6.8 kN (1,518 lb$_f$), roughly the same peak force as the All simulation.
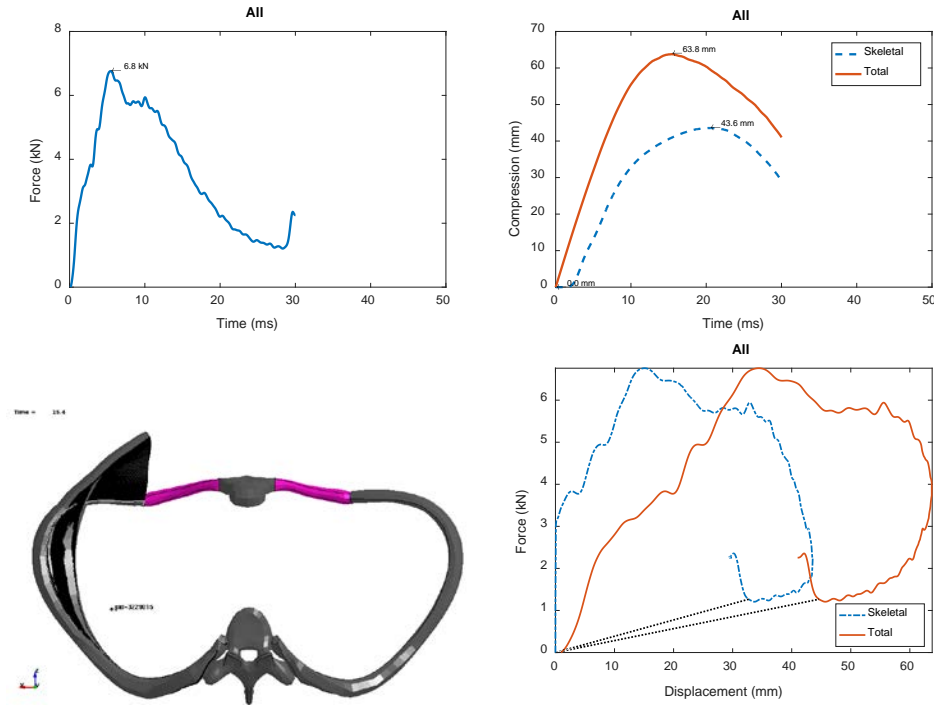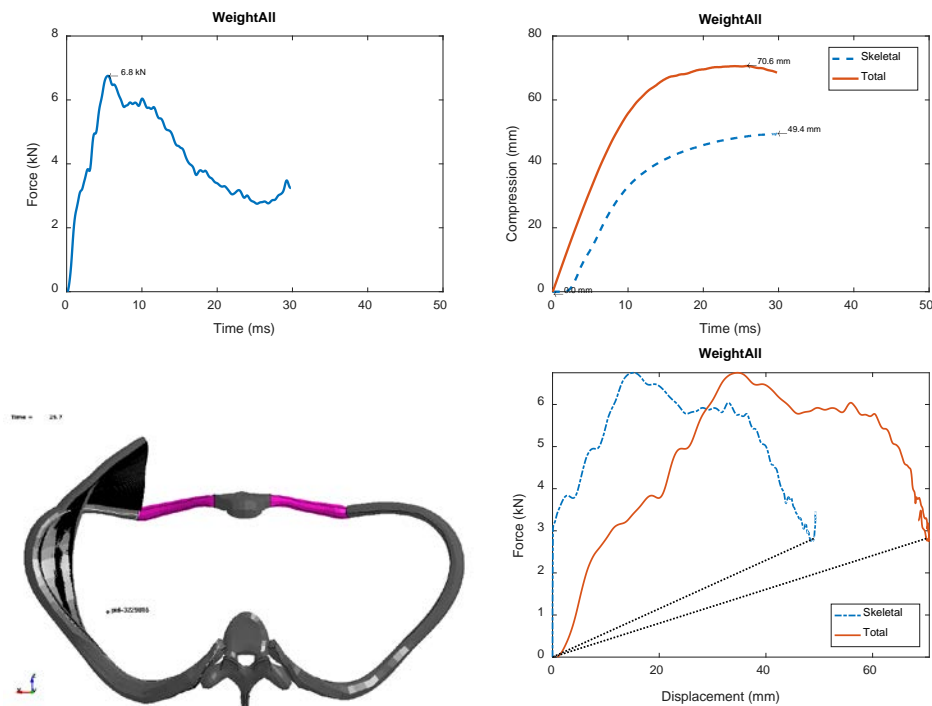

Fig. 25   WeightAll simulation results: force-time (upper left), compression-time (upper right), trace of fifth rib to maximum compression (bottom left), force-displacement (bottom right)
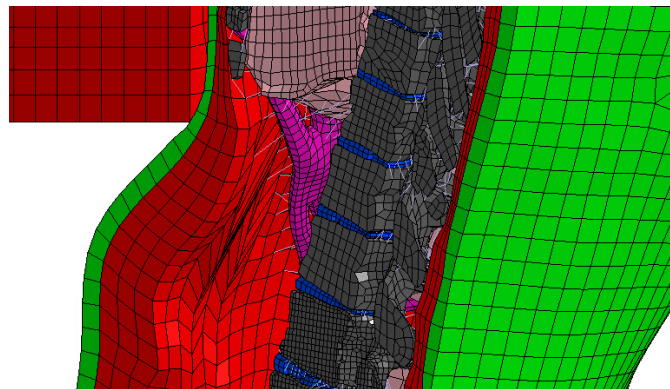
The force-deflection curve was bilinear and showed a force-limited behavior. Very little of the unloading phase was available due to the early termination. The energy absorption was calculated after removing the ending force spike, yielding 69.8% absorption. The actual absorption was likely higher due to the incomplete unloading phase.

Energy distribution at peak compression was 529 J total and 38.3% kinetic, 60.1% internal, and 1.6% sliding energy distribution. Energies were stable until termination. The additional weight restricted the motion of the torso and resulted in a larger share of energy going into internal energy (deformation).

The differences in chest compression between All and WeightAll were driven by the stiffness of the connections to the point masses. As the compliance of the

connections was increased, the results began to resemble those of the All simulation.

Figure 26 shows the response of the torso in 5-ms intervals. The cylinder continually slowed from –6.71 m/s initial velocity to –1.52 m/s. The impactor speed had not leveled off by the termination. The torso was accelerated during impact from rest to –1.8 m/s by 19 ms, after which the velocity remained constant. The increase in compression relative to the Original simulation was more easily visible in the side view, particularly when compared with Fig. 6. Restoring the connectivity and additional weight in the extremities through the point masses was also effective in reducing the rigid body motion of the torso and limited the rotation of both the torso and the cylinder.
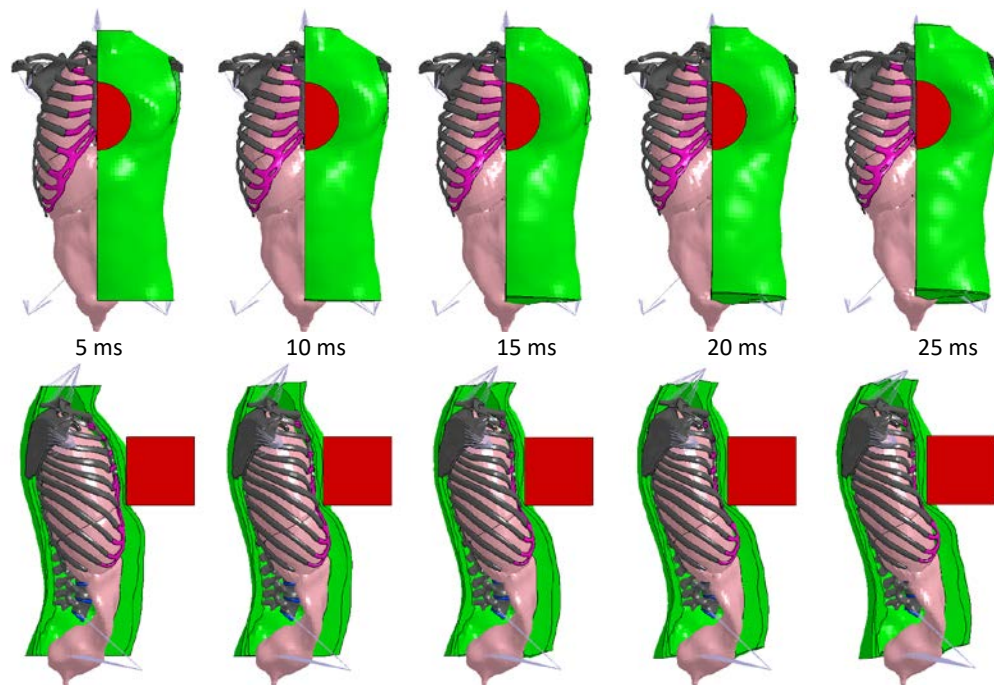
Fig. 26   WeightAll simulation chest response as seen from front (top) and side (bottom). Half of the flesh, skin, and impactor have been hidden to show the bone and organ response.

3.16   WeightEmpty

The final mesh modification simulation, WeightEmpty, was the most extreme, combining the modifications from the WeightAll simulation with the organ removal from the Empty simulation. This simulation approximated the response if the organs were infinitely soft and compressible, without the mesh distortion problems causing the WeightAll simulation to terminate early. With the additional point masses, the organ removal dropped the simulated torso weight by 11.9%, less than the drop between the Original and Empty simulations.

The WeightEmpty simulation terminated early at 25.7 ms due to distorted elements in the abdominal flesh, the same problem elements from previous simulations. As seen in Figs. 27 and 28, the removal of the organs had a dramatic effect on the total compression, which reached 123.9 mm (4.88 inches) at termination. Skeletal compression reached 112.0 mm (4.41 inches). Neither compression had reached peak value by the end of the simulation. The peak force reached 4.4 kN (999 lb$_f$), but this value occurred at termination and was inflated by the simulation instability preceding termination. Ignoring the upward trending force after 20 ms, the peak force was 3.2 kN (712 lb$_f$) at 18.0 ms.
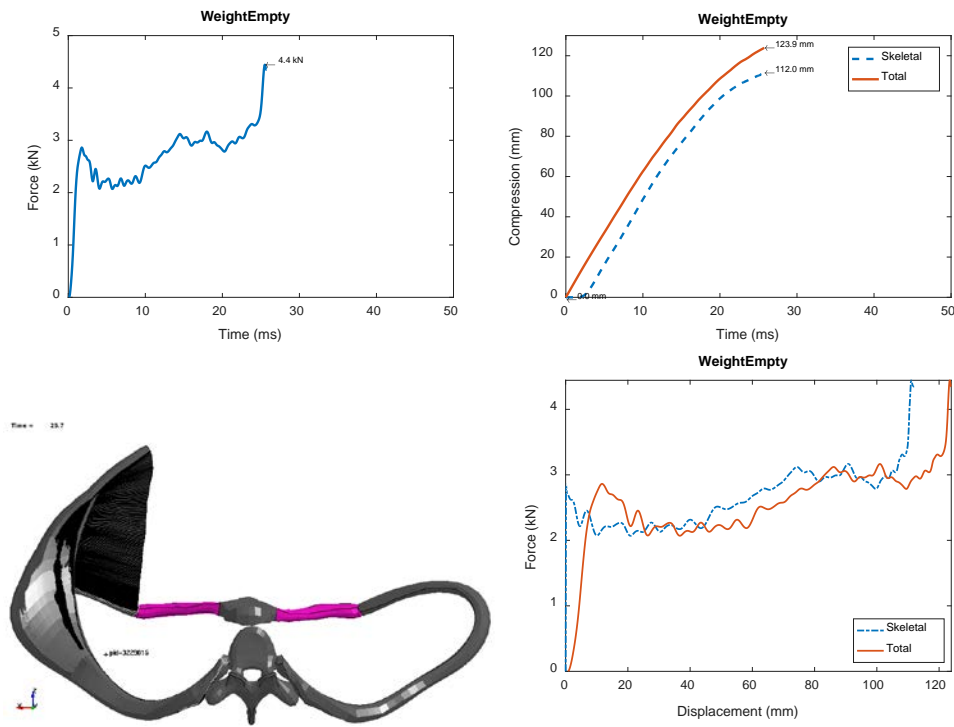
Fig. 27   WeightEmpty simulation results: force-time (upper left), compression-time (upper right), trace of fifth rib to maximum compression (bottom left), force-displacement (bottom right)
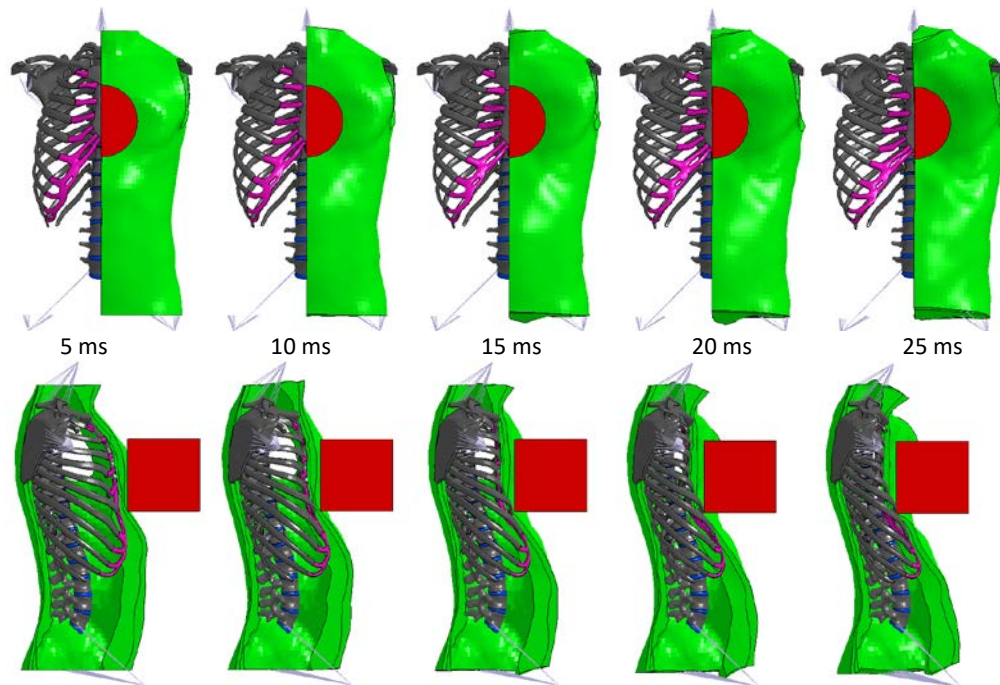
Fig. 28   WeightEmpty simulation chest response as seen from front (top) and side (bottom). Half of the flesh, skin, and impactor have been hidden to show the bone and organ response.

Only the loading phase of the force-deflection curve was available. The behavior was bilinear and force-limited, with a near instantaneous rise to peak force. The absorption could not be calculated due to the missing unloading phase.

The total energy was 529 J, and the energy distribution was 56.3% kinetic, 42.4% internal, and 1.3% sliding energy. Energy was stable until just prior to termination. The removal of the organs and lower weight resulted in a greater share of kinetic energy as was also observed between the Original and Empty simulations.

Figure 28 shows more clearly how the surrounding soft tissue began to wrap around the impactor as the chest compressed. The compression was so extreme that the sternum reached the vertebral column and began to pass through because a contact between the 2 parts was not defined. The impactor slowed from –6.7 m/s to –3.8 m/s just before termination. The torso started from rest and was settling at –1.9 m/s near the simulation end.

4. Discussion

4.1 Simulation Insights

The initial findings from the single modification simulations (Empty, Ribs, Foam, Foam2, NLV, NLV2, Ogden, and Flesh) highlighted how strongly the default linear

elastic material response diverged from the expected nonlinear, viscous biomaterial response. All of the single modification simulations were overly stiff with high peak forces and low chest compressions. The force-deflection curves often displayed increases in force proportional to the chest compressions rather than the desired force plateaus. This behavior is characteristic of the linear elastic material model. There was also minimal energy absorption, which was attributed to the lack of viscous properties.

The single modification simulations predicted that alterations to the soft tissues (organs and flesh) were the most influential. Modifying the flesh material model was the most effective single change to increase total compression and the difference between skeletal and total compression. The modified flesh properties had minimal effect on both the energy absorption and the force-deflection curve shape. Changing the internal organs material to soft foam (Foam2), viscous foam (NLV2), or Ogden rubber (Ogden) formulations was most effective at increasing the energy absorption by obtaining a widened loop and force-limiting behavior in the force-deflection curve. Moderate increases in compression were also obtained, but the increased element deformation degraded simulation stability. Changes to the rib material model had minimal effect since the ribs were constrained between the flesh and organs.

Combining multiple material modifications showed that the changes in compression were not additive. For example, the compression increases from the ComboF simulation were greater than the sum of increased compressions from the Flesh and Foam2 simulations. For these simulations the impact duration and total chest compression were higher, and peak force was lower. Force-limiting and loop-widening features in the force-deflection curves were successfully retained to further increase energy absorption. However, the simulation stability was inversely tied to the compression, and it became increasingly difficult to run simulations long enough to capture the full impact event.

The mesh modification RibShellsAll split the ribs into trabecular in cortical layers. The chest compression was lower than the All simulation because the stiff cortical layer (17 GPa) resulted in a stiffer composite than the homogenized ribs (400 MPa). This composite approach works equally well as the homogenized approach but does not change the need to accurately characterize the material. Restoring the whole body weight in the WeightAll simulation did not affect the impact force. Instead, the peak compression was higher and was sustained for a much longer time than was seen in the isolated torso.

4.2 Comparison with Experiments

Figure 29 compares the force-time, total compression-time, and force-displacement data for the 2 selected PMHS subjects obtained by Kroell et al. (1994) to 3 sets of results from the ARL torso FE model. These results can also be compared to all of the Kroell tests in Fig. 2. The All and WeightAll simulations showed nearly double the peak force despite the similarity in total compression. The WeightEmpty simulation, in which all the internal organs were completely removed, was the only simulation to predict lower peak force than the experiments and predicted drastically higher peak compression.
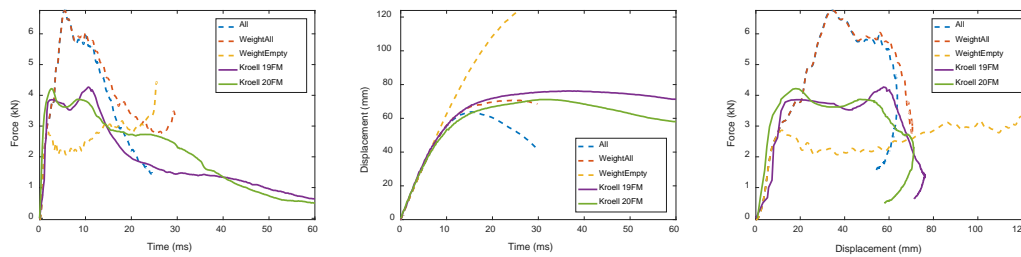
Fig. 29 Comparison of force-time (left), total compression-time (middle), and force-deflection (right) curves from select simulations and Kroell et al. (1994) PMHS 19FM and 20 FM. All impacts are 23.5-kg impactors at 6.7 m/s.

Aside from the high peak force, the shapes of the force-displacement responses were reasonable. The All and WeightAll simulations showed a bilinear loading phase and a wide, energy-absorbing loop like the PMHS experiments. In the initial part of loading, the simulated chest showed similar stiffness but loaded to approximately double the force and compression. In the second part of loading, the simulations showed small decreases in force, whereas the PMHS experiments maintained roughly constant levels of force. Both the experiments and simulations unloaded quickly while the compression remained near peak value.

Simulation peak chest compressions and impactor forces were tabulated in Table 9, sorted from lowest to highest by chest compression. The Foam, NLV, and ComboO simulations were omitted as these simulations terminated before reaching peak compression. The Kroell et al. (1994) results for tests 19FM and 20FM are listed at the bottom of the table for comparison. The results highlighted the inverse relationship between the compression and force. The WeightAll simulation, which predicted 70.6 mm total compression, was the closest to the 71.1- and 76.2-mm compressions in the experiments. As noted before, the 6.8-kN peak force was much higher than the approximately 4.4-kN experimental force. Off-axis impactor forces were less than 10% of the peak axial force, which was in line with the experiments.

Table 9 Peak forces and total compressions sorted by lowest to highest compression

Simulation	Time to peak compression (ms)	Metric units		English units	
		Compression (mm)	Force (kN)	Compression (inches)	Force (lb$_f$)
Original	4.1	20.5	29.9	0.81	6,730
Ribs	4.1	20.8	29.1	0.82	6,543
NLV2	5.4	25.9	20.1	1.02	4,517
Foam2	5.8	27.8	17.1	1.09	3,844
Ogden	6.1	29.6	15.4	1.17	3,462
Empty	6.2	29.9	13.9	1.18	3,135
Flesh	7.3	35.4	19.8	1.39	4,462
ComboN	12.1	49.5	9.9	1.95	2,229
RibShellsAll	12.0	50.7	8.4	2.00	1,895
ComboF	14.3	61.0	7.0	2.40	1,567
All	15.4	63.8	6.8	2.51	1,520
WeightAll	25.7	70.6	6.8	2.78	1,518
WeightEmpty	>25.7	123.9+	3.2	4.88+	719
Kroell 19FM	41.0	76.2	4.3	3.0	960
Kroell 20FM	30.4	71.1	3.9	2.8	1030

The WeightEmpty simulation, which differed from WeightAll by removing the internal organs, drastically overpredicted the peak compression and underpredicted the peak force. The bulk compressive properties of the organs, which lay inside the chest cavity, mitigate the total compression by preventing the ribs from flexing. This also increased the energy absorption by minimizing the energy going into the elastic ribs.

Table 10 shows the unsorted energy absorption in the force-deflection loop. The Foam, NLV, Ogden, ComboO, and WeightEmpty simulations had incomplete force-deflection loops and were excluded. While the energy absorption improved from 33.2% in the Original simulation to 79.2% in the All simulation, no simulation could match the 89% absorption from the experiments. The lower absorption in the WeightAll simulation could be due to the force-deflection loop being less complete than in the All simulation. The extremely low unloading phase energies in the experiments showed how little elasticity was in the PMHS chest response.

Table 10 Breakdown of force-displacement curves by loading area, unloading area, and percent of energy absorbed during impact

Simulation	Loading phase (J)	Unloading phase (J)	Energy absorbed (%)
Original	314.7	210.1	33.2
Empty	277.4	250.8	9.6
Ribs	316.9	206.7	34.8
Foam2	320.3	225.2	29.7

Table 10 Breakdown of force-displacement curves by loading area, unloading area, and percent of energy absorbed during impact (continued)

Simulation	Loading phase (J)	Unloading phase (J)	Energy absorbed (%)
NLV2	328.9	184.4	43.9
Flesh	266.7	104.4	60.9
ComboF	297.7	75.2	74.8
ComboN	287.1	59.8	79.2
All	298.2	62.1	79.2
RibShellsAll	284.5	109.1	61.7
WeightAll	331.4	100.2	69.8
Kroell 19FM	243.9	27.1	88.9
Kroell 20FM	241.7	27.2	88.7

Simulations that predicted higher total chest compression tended to have higher energy dissipation and lower loading and unloading energy values. However, the loading energy was also correlated to the total body mass. Loading energy dropped in the Empty simulation (organs removed) and increased in the WeightAll simulation (added mass for limbs). The lowest energy absorption (9.6%) was from the Empty simulation because the response was dominated by rib flexion, and the ribs were characterized with an elastic material. All of the loading phase energies were higher in the simulations than in the experiments due to the higher impactor forces. However, this could also be influenced by velocity loss in the impactor between launch and impact. The effect from such an error would be magnified as energy is proportional to the square of velocity.

4.3 Organ Material Models

Each of the 3 material models for internal organs had its strengths and weaknesses. The low-density foam (Mat57) was the easiest to stabilize due to its piecewise stress-strain input curve, but it also increased the computational cost of the simulation by 4 times. The biphasic nonlinear viscoelastic model (Mat62) was far more computationally efficient but only crudely represented the exponential-like response of soft tissues and resulted in less chest compression. Finally, the Ogden model (Mat77O) offered the highest compression, but the implementation did not readily allow for stiffening the response at high strains needed to stabilize the simulations. Additionally, all of the material models lacked rate sensitivity.

The heart and lungs were heavily compressed under impact. This introduced a significant challenge unique to the discretized mesh scheme used in FE analysis: mesh distortion. Individual elements became thinned and warped with increasing compression, altering the element time step and stiffness. This also increased the time needed to run the simulation and sometimes resulted in an error termination.

Adapting the mesh to accommodate the expected compression was not feasible due to the complex geometry of the organs. Some possible alternatives to the traditional Lagrangian meshes for future simulations may be to adapt a hollow shell implementation, to replace the organs with closed shells containing a control volume, or to implement a local Eulerian subdomain within the organ. These alternatives may allow for greater localized deformation without negatively affecting the simulation stability.

Figure 30 shows an example of the heart undergoing substantial compression and flattening as the sternum was pushed inwards. The most extreme case, a modified version of the WeightAll simulation in which the lungs were removed, shows the posterior side of the heart beginning to wrap around the vertebral column. The difference between the WeightAll and modified WeightAll simulations highlights the importance of empty volumes and adjacent structures in the chest and organ response.
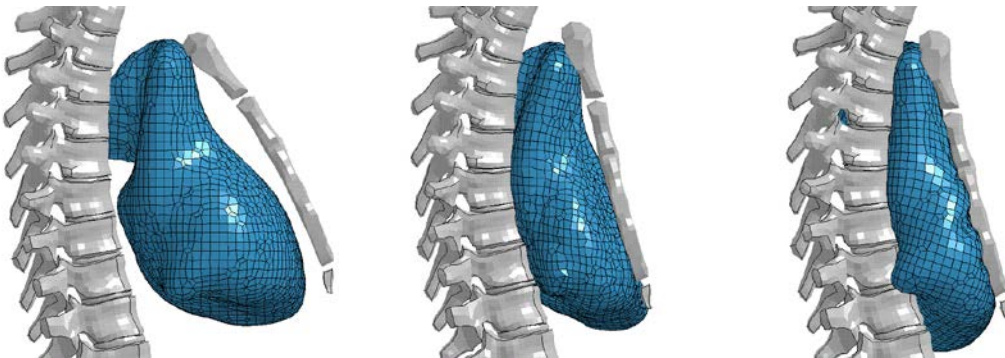
Fig. 30   Compression of the heart pre-impact (left), at peak compression in the WeightAll simulation (middle), and a modified simulation with the lungs removed (right). Only the heart, vertebral column, and sternum are shown to improve visibility.

In the WeightAll simulation, the anterior surface developed grooves from localized rib impingement. Kroell et al. (1994) attributed visceral injuries and increased chest compression in PMHS to this localized loading, resulting in lacerating rib fractures. The current ARL torso model did not allow for rib fracture. This limited the peak compression but also improved the simulation stability by reducing mesh distortion and minimizing free contact edges. In the long term, the model will need the capability to simulate both rib fracture and the interaction between the broken edges and nearby structures to improve the biofidelity of the model.

One limitation of the FE model was the lack of a vascular system. Kroell et al. (1994) pressurized the heart and aortic arch of PMHS 20FM with water, recording 25 mmHg prior to impact and roughly 800 mmHg peak during the impact. In vivo, the heart and vasculature would be filled with viscous fluids. The pressure

differential generated by impact could be temporarily driving fluid out the impacted organs, resulting in a transient increase in chest compliance. The Lagrangian nature of the FE method makes it difficult to evaluate such fluid flows. In the future, it might be possible to account for these flows by representing the organs with control volumes or implementing an Eulerian background behind hollow organs.

4.4 Chest Measurement Limitations

Variance in the chest depth was a possibly significant factor in the chest response that was not controlled for in the experimental study or the simulations. The 2 specimens selected from Kroell et al. (1994) both had chest depths of 8 inches (203 mm). This was lower than the ARL torso chest depth of 235.8 mm (9.3 inches). Since chest compression could be assumed to scale up with increasing chest depth, this suggested that the error between the simulations and experimental results might be somewhat larger than initially thought. For example, the percent error in total compression between the WeightAll simulation and the 20FM PMHS experiment was only –0.7% but increased to –14.5% when calculated as the error in the percentage of chest compression. Scaling the ARL torso size to match the available external measures could be done for future studies but would require insight into how the size and positioning of internal structures change with chest size.

The difficulties in adjusting posture in the FE model resulted in different postures between the experiment (Fig. 1) and simulation (Fig. 3). The typical PMHS specimen was characterized by raised shoulders, a rounded back, and a flat frontal chest profile. This maximized the visibility of the markers and minimized the off-axis impactor forces. The ARL torso model had a more upright posture characterized by drawn-back shoulders, a neutral spinal curvature, and a sloped chest profile. The ARL torso model posture caused the back to be recessed 15.4 mm relative to the shoulder and the chest center 8.9 mm relative to the pectorals. The presence of recesses on the PMHS chest was not recorded and might affect the 2-D video compression measurements. Referring to Fig. 1, the posture appeared to remove any back recess but might increase the chest recession.

Alternative measurements were made to evaluate the effect of recesses and initial gaps in the ARL torso model using additional measurement points described in Fig. 4. The effect upon the force-displacement curve for the WeightAll simulation is shown in Fig. 31. Using the shoulder as the rear measurement point instead of the back resulted in an additional 5.9 mm (0.23 inches) to both compressions caused by the arm weight pulling the shoulders forward. Using the impactor as the front measurement point instead of the chest center increased total compression 12.5 mm

(0.49 inches). This is similar to the 11.5-mm (0.45-inch) gap between the cylinder center of gravity and pectoral surface, although the sloped chest surface causes the initial separation to range between 1.2 and 54.4 mm (0.0 and 2.1 inches). The initial separation between the impactor and chest heavily influenced the force-deflection slope at the beginning of the impact. Skeletal and total measurements using the chest as the frontal point were all characterized by near-instant rises in force, whereas impactor-based total compressions were more gradual. Most of the PMHS compressions were also gradual, which might be caused by chest recesses or variations in posture creating initial separation.
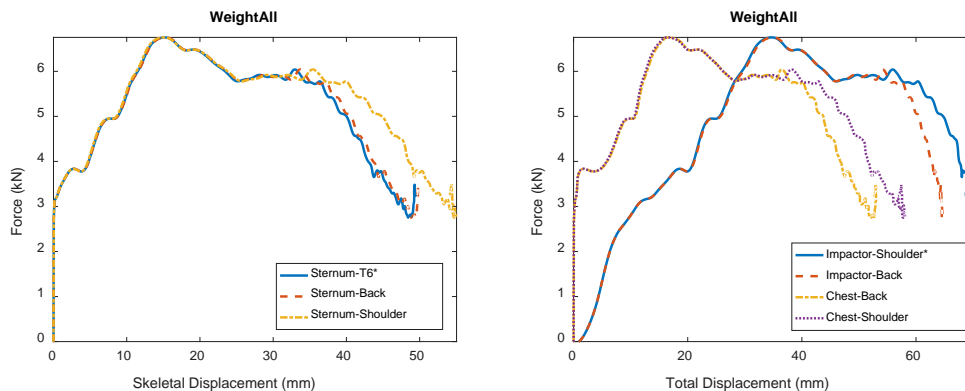
Fig. 31 Force-displacement results for WeightAll simulation using different points to measure skeletal and total compressions. The asterisk marks the measurements presented in the Results section.

Kroell et al. (1994) discussed in detail the limitation of using the total compression measured by video tracking as a proxy to the skeletal compression used in previous studies (Kroell et al. 1994; Nahum et al. 1970) due to variations in soft tissues overlaying the skeletal structures. It was suggested that skeletal compression would usually be 0.5 to 0.75 inches (12.7 to 19.1 mm) lower than the total compression, with the discrepancy being larger for female and overweight specimens with larger amounts of soft tissue. The difference for the ARL torso was 21.2 mm (0.83 inches) in the WeightAll simulation. The measurement differential was driven by the flesh material model and the relative softness between the flesh and other body regions. The Flesh simulation, with soft flesh and relatively stiff organs, had the highest difference (23 mm). The WeightEmpty simulation used the same soft flesh, but the empty chest cavity made the flesh relatively stiff, and as a result had a lower difference (11.9 mm).

4.5 Simulation Performance

General simulation information shown in Table 11 revealed that the original simulation required a little under 14 hours to complete the full 50-ms simulated time. Distribution of the computation cycles tended to be around 60% for contacts and 20% for elements, with the remaining distributed over communication and input/output demands. Simulations that terminated early due to errors, such as Foam, NLV, and Ogden, tended to have reasonable time steps and progress rates until they neared termination. Thus, these simulations had progression rates slightly higher than documented.

Table 11 Summary of simulation costs

Simulation	Ending sim time (ms)	Wall time (h)	Rate (ms/h)
Original	50.0	13.8	3.6
Empty	50.0	6.7	7.5
Ribs	50.0	11.1	4.5
Foam	4.4	1.4	3.2
Foam2	50.0	38.5	1.3
NLV	3.1	0.8	4.0
NLV2	50.0	10.8	4.7
Ogden	7.7	2.5	3.1
Flesh	22.3	5.5	4.1
ComboF	30.6	22.1	1.4
ComboN	31.4	7.9	4.0
ComboO	8.4	2.7	3.1
All	30.0	25.5	1.2
RibShellsAll	21.2	14.6	1.5
WeightAll	29.8	27.1	1.1
WeightEmpty	25.7	5.7	4.5

Removal of the organs in the Empty simulation provided a 105% boost to the progress rate due to the elimination of many contacts and elements. On the other hand, the use of the soft foam material in the Foam2 simulations incurred a substantial 64% reduction in the progress rate. Time step reductions tended to be driven by either element warping, which reduced the element size, or element stiffening under high stretch, which increased the wave speed. As a result, the time step fell to remain below the time needed for a wave to pass through the element.

4.6 Energy Balances

Figure 32 shows the distributions of internal energies for the various simulations. For most simulations, the internal organs and soft tissues absorbed most of the impact energy. Removal of the internal organs in the Empty and WeightEmpty

simulations caused the energy to redistribute among the remaining components with preference toward the flesh and skin. Simulations with higher total compression tended to deposit a greater share of internal energy into the organs and less in the flesh and skin. The additional weight added to the WeightAll and WeightEmpty simulations increased the internal energy share of the bones and ligaments to which the extra weights were connected.
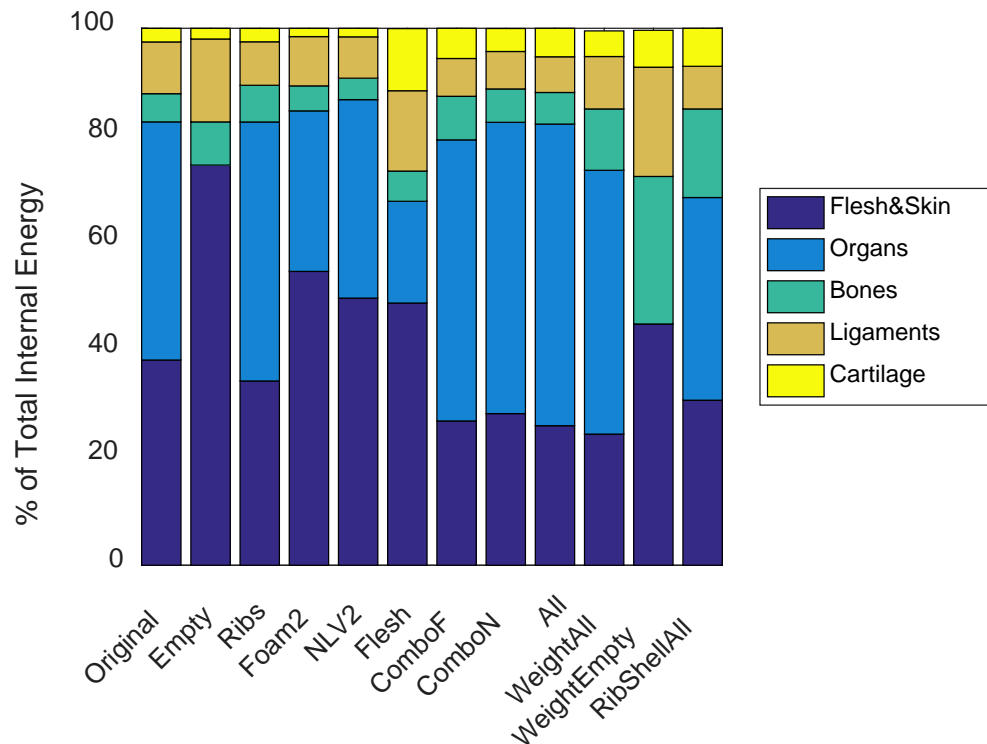
Fig. 32   Distribution of internal energy between various materials of the body at peak internal energy

5. Conclusions

The key performance metrics for the ARL torso finite element model in a frontal chest impact were greatly improved by adding additional mass to approximate the extremities and altering the material models for the ribs, homogenized flesh, and internal organs (Table 12). The most influential change was switching from elastic to nonlinear viscous material models although the improvements still fall slightly short of the experimental results in peak force and energy absorption. Qualitatively, the force-displacement curve successfully transitioned from a narrow elastic loop toward a wider, bilinear loop. In general, the simulation stability was inversely related to the peak total compression, which poses a challenge for future studies interested in further improving the model or simulating more severe impacts.

Table 12   Key numerical metrics for assessing simulation performance

Metric	Averaged PMHS	Original simulation	WeightAll simulation
Peak force (kN)	4.4	29.9	6.8
Peak compression (mm)	73.6	20.5	70.6
Energy absorption	88.8%	33.2%	69.8%

Avenues for future improvements include scaling and posturing the ARL torso, new material models, and alternative methods to represent the organs. The current soft foam model used for the organs in this study was the best at accommodating large deformations but came with a substantial computational cost. Improved stabilization of the organs, whether through new material models or alternative representations, is needed to capture increased impact severities. Anthropometric variables including size, posture, and age are also needed as experimental studies tend to have fewer subjects with a wide range of variability.

6. References

Bass CR, Salzar RS, Lucas SR, Davis M, Donnellan L, Folk B, Sanderson E, Waolawik S. Injury risk in behind armor blunt thoracic trauma. International Journal of Occupational Safety and Ergonomics. 2006;12(4):429–442.

Cannon L. Behind blunt armor trauma – an emerging problem. Journal of the Royal Army Medical Corps. 2001;147:87–96.

Carr DJ, Horsfall I, Malbon C. Is behind armor blunt trauma a real threat to users of body armor? A systemic review. Journal of the Royal Army Medical Corps. 2016;162(1):8–11.

Clauser CE, McConville JT, Young JW. Weight, volume, and center of mass of segments of the human body. Wright-Patterson AFB (OH): Air Force Systems Command (US); 1969. Report No.: AD-710 622.

Cormier JM, Stitzel JD, Duma SM, Matsuoka F. Regional variation in the structural response and geometrical properties of the human ribs. Association for Advances in Automotive Medicine. 2005;49:153–170.

Dong L, Zhu F, Jin X, Suresh M, Jiang B, Sevagan G, Cai Y, Li G, Yang KH. Blast effect on the lower extremities and its mitigation: a computational study. Journal of the Mechanical Behavior of Biomedical Materials. 2013;28:111–124.

Goldfarb MA, Clurej TF, Weinstein MA, Metker RW. A method for soft body armor evaluation: medical assessment. Aberdeen Proving Ground (MD): Edgewood Arsenal (US); 1975. Report No.: EB-TR-74073.

Government Accountability Office. Personal protective equipment: Army and Marine Corps are pursuing efforts to reduce the weight of items worn or carried into combat. Washington (DC): Government Accountability Office; 2017. Report No.: GAO-17-431.

Government Publishing Office. 2011 Code of Federal Regulations: Title 49 – Transportation: Part 572 – Anthropomorphic Test Devices. Washington (DC): Government Publishing Office; 2011. Report CFR-2011-title49-vol7-part572.

Hampton CE, Kleinberger M. Evaluation of injury protection provided by boots in axial impacts. Proceedings of the 43rd Northeast Bioengineering Conference; 2017; Newark, NJ.

Hanlon E, Gillich P. Origin of the 44-mm behind-armor blunt trauma standard. Military Medicine. 2012;177:333–339.

Kroell CK. Thoracic response to blunt frontal loading in biomechanics of impact injury and injury tolerances of the thorax-shoulder complex. Backaitis SH, editor. Society of Automotive Engineers International PT-45. Warrendale (PA): SAE, Inc.; 1994. p. 51–79.

Kroell CK, Schneider DC, Nahum AM. Impact tolerance and response of the human thorax in Biomechanics of impact injury and injury tolerances of the thorax-shoulder complex. Backaitis SH, editor. Society of Automotive Engineers International PT-45. Warrendale (PA): SAE, Inc.; 1994. p. 133–181.

Lee JB, Yang KH. Development of a finite element model of the human abdomen. Stapp Car Crash Journal. 2001;45:79–100.

Livermore Software Technology Corporation (LSTC). LS-DYNA keyword user's manual. Release 9.0. Livermore (CA): Livermore Software Technology Corporation (LSTC); 2016.

Lynch ML, Wozniak SL, Sokolow A. Material parameter sensitivity of predicted injury to the lower leg. Aberdeen Proving Ground (MD): Army Research Laboratory (US); 2015. Report No.: ARL-TR-7310.

Merkle AC, Ward EE, O'Connor JV, Roberts JC. Assessing behind armor blunt trauma (BABT) under NIJ Standard-0101.04 conditions using human torso models. Journal of Trauma. 2008;64(6):1555–1561.

Mukasey MB, Sedgwick JL, Hagy DW. Ballistic resistance of body armor. Washington (DC): Department of Justice (US); 2008. NIJ Standard-0101.06 [accessed 2018 Mar 1]. https://www.ncjrs.gov/pdffiles1/nij/223054.pdf.

Nahum AM, Gadd CW, Schneider DC, Kroell CK. Deflection of the human thorax under sternal impact. SAE Technical Paper 700400. Proceedings of the International Automobile Safety Conference; 1970; Detroit, MI.

Naini AS, Patel RV, Samani A. Measurement of lung hyperelastic properties using inverse finite element approach. IEEE Transactions on Biomedical Engineering. 2011;58(10):2852–2859.

Prather RN, Swann CL, Hawkins CE. Backface signatures of soft body armors and the associated trauma effects. Aberdeen Proving Ground (MD): Army Armament Research and Development Command (US); 1977. Report No.: ARCSL-TR-77055.

Rater JF. Thorax soft tissue response for validation of human body models and injury prediction [thesis]. [Gothenburg (Sweden)]: Chalmers University of Technology; 2013.

Shigeta K, Kitagawa Y, Yasuki T. Development of next generation human FE model capable of organ injury prediction. Enhanced Safety of Vehicles Paper 09-0111; 2009.

Snedeker JG, Bajka M, Hug JM, Szekely G, Niederer P. The creation of a high-fidelity finite element model of the kidney for use in trauma research. Computer Animation and Virtual Worlds. 2002;13(1):53–64.

Sokolow A. Progress in finite element modeling of the lower extremities. Aberdeen Proving Ground (MD): Army Research Laboratory (US); 2015. Report No.: ARL-MR-0890.

Stojsih S. A biomechanical assessment of canine body armor [dissertation]. [Detroit (MI)]: Wayne State University Paper 1296. 2015 [accessed 2017 June 20]. http://digitalcommons.wayne.edu/oa_dissertations/1296/.

Untaroiu CD, Lu YC. Material characterization of liver parenchyma using specimen-specific finite element models. Journal of the Mechanical Behavior of Biomedical Materials. 2013;26:11–22.

Zygote Media Group Inc. Zygote Solid 3-D Male Anatomy Collection Generation II Development Report. American Fork (UT): Zygote Media Group Inc.; 2015.

Appendix. Army Research Laboratory Torso Parts and Mesh Quality Report

The US Army Research Laboratory torso finite element model (build 2017 Aug 01) contained 271 parts consisting of 207,521 elements and 243,558 nodes. Solid elements representing bulk tissue were contained in 90 parts containing 187,727 hexahedral brick elements. The list of parts, number of elements per part, and basic quality metrics were summarized in Table A-1. For each part the available quality metrics were the lowest element volume (Vmin), the minimum edge length, which influenced time step (Lmin), and the minimum and maximum interior element angles (θmin and θmax).

The remaining 181 parts represented the connective ligaments and contained 19,794 beam elements. These parts were summarized in Table A-2. There were no quality metrics for these elements because the implementation was that of a simplified 1-D beam. Ligaments were automatically generated by a script that connects nodes from 2 different parts when they were less than a threshold distance from each other and not already used to make a different ligament.

Table A-1   List of parts containing solid elements with quality metrics

Part name	Part ID	No. elem	Vmin	Elem no.	Lmin	Elem no.	θmin	Elem no.	θmax	Elem no.
c L1 disc	2259001	708	4.6	19	0.79	24	25.2	19	161	28
c L1 vertebra	2229001	6879	0.43	5776	0.42	5774	12.7	5776	164	5776
c L2 disc	2259002	348	13	7752	1.2	7599	30.6	7890	142	7608
c L2 vertebra	2229002	7094	0.35	13439	0.39	9122	14.2	9122	173	12208
c L3 disc	2259003	456	7.7	15371	1.2	15055	21.4	15281	149	15056
c L3 vertebra	2229003	7326	0.23	19972	0.38	15576	14.4	19970	156	22779
c L4 disc	2259004	540	2.8	23129	0.96	22976	14	23159	158	22976
c L4 vertebra	2229004	8014	0.73	30185	0.42	29071	15.1	27652	154	29823
c L5 disc	2259005	624	5.4	31539	0.8	31607	9.79	31948	158	31485
c L5 vertebra	2229005	7317	1	37385	0.46	32399	9.9	32343	163	36993
c T10 disc	2259110	208	10	39309	0.92	39315	34.7	39316	133	39457
c T10 vertebra	2229310	776	8	39631	1	40019	12.1	40247	159	39788
c T11 disc	2259111	436	4.8	40439	1	40438	18.2	40305	157	40439
c T11 vertebra	2229311	618	23	40745	1.8	41054	11.7	41342	157	41112
c T12 disc	2259112	500	3.3	41598	0.81	41394	27.9	41571	153	41694
c T12 vertebra	2229312	938	18	41943	1.4	42300	12.5	41991	158	42512
c T1 disc	2259101	216	1.2	42831	0.42	42784	17.4	42947	154	42981
c T1 vertebra	2229301	958	4	43362	1.1	43233	8.52	43109	156	43220
c T2 disc	2259102	608	0.45	44202	0.22	44008	23.1	44432	154	44024
c T2 vertebra	2229302	1320	5.2	44586	1.1	45034	10.3	45719	158	44732
c T3 disc	2259103	672	0.67	45946	0.44	45983	27.5	45982	160	46292
c T3 vertebra	2229303	1248	4.2	46564	1.1	46557	8.82	46715	158	46564
c T4 disc	2259104	608	0.67	48240	0.53	47875	21.3	48280	159	47874
c T4 vertebra	2229304	2104	3	49437	1	48468	10.9	48489	160	48643
c T5 disc	2259105	304	2.6	50745	0.52	50549	28.5	50749	143	50541

Part name	Part ID	No. elem	Vmin	Elem no.	Lmin	Elem no.	θmin	Elem no.	θmax	Elem no.
c T5 vertebra	2229305	1612	3.8	51929	1	50936	9.95	50900	157	51352
c T6 disc	2259106	152	5.5	52548	1.2	52452	35.1	52487	130	52510
c T6 vertebra	2229306	1622	3.5	53101	1	53145	11.1	54165	158	52807
c T7 disc	2259107	304	3.6	54434	0.83	54294	36.2	54259	136	54270
c T7 vertebra	2229307	744	23	54644	1.3	54557	13.6	54985	159	54568
c T8 disc	2259108	388	1.5	55296	0.62	55299	20.8	55269	156	55269
c T8 vertebra	2229308	644	21	55773	1.5	55789	12.8	56119	159	55907
c T9 disc	2259109	152	10	56384	0.62	56294	33.9	56384	133	56392
c T9 vertebra	2229309	540	21	56497	1.3	56897	12.9	56806	159	56743
c cylinder	2229999	2560	190	185335	3.2	185704	29.2	185626	136	185689
c heart	2289001	7136	7.5	62528	1.1	62525	8.37	59768	174	63625
c intestine	2289002	22515	2.6	85679	0.86	73013	15.9	73431	156	80854
c left kidney	2289005	688	52	86657	2.5	87311	16.9	87298	155	87149
c left lung	2289004	22070	1.5	104146	0.76	100198	6.92	102391	168	102394
c liver gall	2289008	13406	3.8	109493	1	112190	10.4	119519	165	110669
c pancreas	2289007	1328	15	123149	1.1	123065	11.1	123152	157	123462
c right kidney	2289006	864	33	124216	2	124153	14.3	124846	151	124867
c right lung	2289003	8855	13	133678	1.4	133514	13.2	133585	164	131698
c spleen	2289010	4407	8.4	137378	1.4	136880	7.83	137458	159	137543
c sternumA	2229401	388	21	138252	1.9	138297	11.1	138557	154	138328
c sternumB	2229402	880	9.7	139067	1.7	138642	12.7	139495	157	138746
c sternumC	2229403	8	29	139520	2.3	139520	30.4	139518	134	139520
c stomach	2289009	1940	8	139996	1.1	139996	11.7	140071	156	141347
c torso flesh	2239030	16656	41	147283	0.46	144246	5.09	149499	170	147375
c torso skin	2289029	5552	110	158412	0.98	158854	9.91	162589	162	158601
l clavicle	3229028	1634	5.2	164190	1.2	163877	17.7	164330	158	164541
l costal 1	3279021	36	58	165312	2.6	165307	31.4	165341	125	165329
l costal 2	3279022	86	15	165388	1.4	165365	20.4	165411	150	165344
l costal 3	3279023	66	33	165430	2	165440	27.1	165432	151	165435
l costal 4	3279024	116	20	165592	1.6	165498	18.5	165497	157	165518
l costal 5	3279025	86	29	165665	1.8	165640	15.1	165653	150	165651
l costal 6	3279026	972	6.1	166450	1.2	166450	11	165923	156	166562
l rib 1	3229011	156	28	166722	2.3	166815	17.4	166811	157	166682
l rib 10	3229020	284	27	166961	2	166887	19.5	166863	157	166987
l rib 11	3229021	177	30	167272	2	167272	16.9	167139	146	167111
l rib 12	3229022	122	15	167333	1.8	167315	17.8	167307	158	167339
l rib 2	3229012	272	25	167500	2.1	167526	17.6	167428	145	167580
l rib 3	3229013	278	23	167830	1.9	167818	18.8	167705	152	167818
l rib 4	3229014	264	44	168036	1.2	168192	12.1	168215	163	168206
l rib 5	3229015	282	42	168230	2.2	168274	10.3	168396	157	168395
l rib 6	3229016	264	49	168528	2.1	168672	14	168649	151	168506
l rib 7	3229017	282	44	168780	2.1	168789	13.2	168795	157	168800
l rib 8	3229018	276	34	169087	2.3	169217	24.6	169282	147	169110
l rib 9	3229019	302	37	169340	2.1	169457	16.6	169391	155	169490

Table A-1   List of parts containing solid elements with quality metrics (continued)

Part name	Part ID	No. elem	Vmin	Elem no.	Lmin	Elem no.	θmin	Elem no.	θmax	Elem no.
l scapula	3229027	4841	2.4	174269	0.52	172048	9.01	174401	163	170869
r clavicle	1229028	1634	5.2	174986	1.2	174673	9.23	175861	158	175337
r costal 1	1279021	36	58	176108	2.6	176103	35.6	176131	125	176125
r costal 2	1279022	86	15	176184	1.4	176161	26.2	176207	150	176140
r costal 3	1279023	66	33	176226	2	176236	24.7	176237	151	176231
r costal 4	1279024	116	20	176388	1.6	176294	14.9	176291	157	176318
r costal 5	1279025	86	29	176461	1.8	176436	14.8	176463	150	176447
r costal 6	1279026	972	6.1	177246	1.2	177246	8.32	177188	156	176847
r rib 1	1229011	156	28	177518	2.3	177611	15.9	177611	157	177478
r rib 10	1229020	284	27	177757	2	177683	19.5	177659	157	177783
r rib 11	1229021	177	30	178068	2	178068	18.3	178069	146	177907
r rib 12	1229022	122	15	178129	1.8	178111	12.2	178093	158	178135
r rib 2	1229012	272	25	178296	2.1	178322	17.2	178368	145	178376
r rib 3	1229013	278	23	178626	1.9	178614	16.7	178646	163	178617
r rib 4	1229014	264	44	178832	1.2	178988	7.8	179003	163	179002
r rib 5	1229015	282	42	179026	2.2	179070	15.6	179107	157	179191
r rib 6	1229016	264	49	179324	2.1	179468	16.9	179368	151	179431
r rib 7	1229017	282	44	179883	2.1	179585	16	179577	157	179596
r rib 8	1229018	276	34	179883	2.3	180013	22.2	179847	147	179907
r rib 9	1229019	302	37	180136	2.1	180253	16.2	180187	155	180286
r scapula	1229027	4841	2.4	185065	0.52	182844	7.1	180967	160	180493

Table A-2   List of parts containing beam elements

Part name	Part ID	No. of elements
Ligc L1 vertebrac T12 vertebra	490092	170
Ligc L2 vertebrac L1 vertebra	490091	700
Ligc L3 vertebrac L2 vertebra	490090	617
Ligc L4 vertebrac L3 vertebra	490089	659
Ligc L5 vertebrac L4 vertebra	490088	757
Ligc T10 vertebrac T9 vertebra	490095	173
Ligc T10 vertebral rib 10	490065	29
Ligc T10 vertebrar rib 10	490022	29
Ligc T11 vertebrac T10 vertebra	490094	131
Ligc T11 vertebral rib 11	490066	23
Ligc T11 vertebrar rib 11	490023	23
Ligc T12 vertebrac T11 vertebra	490093	147
Ligc T12 vertebral rib 12	490067	27
Ligc T12 vertebrar rib 12	490024	27
Ligc T1 vertebral rib 1	490056	38
Ligc T1 vertebrar rib 1	490013	38
Ligc T2 vertebrac T1 vertebra	490103	161
Ligc T2 vertebral rib 2	490057	41

Table A-2   List of parts containing beam elements (continued)

Part name	Part ID	No. of elements
Ligc T2 vertebrar rib 2	490014	41
Ligc T3 vertebrac T2 vertebra	490102	205
Ligc T3 vertebral rib 3	490058	53
Ligc T3 vertebrar rib 3	490015	53
Ligc T4 vertebrac T3 vertebra	490101	269
Ligc T4 vertebral rib 4	490059	47
Ligc T4 vertebrar rib 4	490016	47
Ligc T5 vertebrac T4 vertebra	490100	277
Ligc T5 vertebral rib 5	490060	42
Ligc T5 vertebrar rib 5	490017	42
Ligc T6 vertebrac T5 vertebra	490099	250
Ligc T6 vertebral rib 6	490061	42
Ligc T6 vertebrar rib 6	490018	42
Ligc T7 vertebrac T6 vertebra	490098	242
Ligc T7 vertebral rib 7	490062	43
Ligc T7 vertebrar rib 7	490019	43
Ligc T8 vertebrac T7 vertebra	490097	187
Ligc T8 vertebral rib 8	490063	33
Ligc T8 vertebrar rib 8	490020	33
Ligc T9 vertebrac T8 vertebra	490096	152
Ligc T9 vertebral rib 9	490064	35
Ligc T9 vertebrar rib 9	490021	35
Ligc left lungc heart	490106	899
Ligc left lungc liver gall	490107	253
Ligc liver gallc intestine	490112	31
Ligc liver gallc pancreas	490109	56
Ligc liver gallc right kidney	490111	95
Ligc liver gallc spleen	490110	41
Ligc liver gallc stomach	490108	307
Ligc pancreasc intestine	490116	139
Ligc pancreasc spleen	490117	95
Ligc right lungc heart	490104	421
Ligc right lungc liver gall	490105	273
Ligc spleenc intestine	490118	157
Ligc spleenc left kidney	490119	47
Ligc sternumAc sternumB	490001	4
Ligc sternumCc sternumB	490002	7
Ligc stomachc intestine	490115	97
Ligc stomachc pancreas	490113	123
Ligc stomachc spleen	490114	147
Ligc torso fleshc L1 vertebra	490120	17
Ligc torso fleshc L2 vertebra	490121	14
Ligc torso fleshc L3 vertebra	490122	14
Ligc torso fleshc L4 vertebra	490123	11
Ligc torso fleshc L5 vertebra	490124	9

Table A-2   List of parts containing beam elements (continued)

Part name	Part ID	No. of elements
Ligc torso fleshc T10 vertebra	490125	26
Ligc torso fleshc T11 vertebra	490126	27
Ligc torso fleshc T12 vertebra	490127	18
Ligc torso fleshc T1 vertebra	490128	23
Ligc torso fleshc T2 vertebra	490129	25
Ligc torso fleshc T3 vertebra	490130	17
Ligc torso fleshc T4 vertebra	490131	13
Ligc torso fleshc T5 vertebra	490132	14
Ligc torso fleshc T6 vertebra	490133	24
Ligc torso fleshc T7 vertebra	490134	28
Ligc torso fleshc T8 vertebra	490135	28
Ligc torso fleshc T9 vertebra	490136	29
Ligc torso fleshc intestine	490137	730
Ligc torso fleshc sternumA	490138	44
Ligc torso fleshc sternumB	490139	72
Ligc torso fleshc sternumC	490140	10
Ligc torso fleshl clavicle	490141	72
Ligc torso fleshl costal 1	490142	7
Ligc torso fleshl costal 2	490143	22
Ligc torso fleshl costal 3	490144	25
Ligc torso fleshl costal 4	490145	31
Ligc torso fleshl costal 5	490146	34
Ligc torso fleshl costal 6	490147	160
Ligc torso fleshl rib 1	490148	1
Ligc torso fleshl rib 10	490149	93
Ligc torso fleshl rib 11	490150	72
Ligc torso fleshl rib 12	490151	29
Ligc torso fleshl rib 2	490152	15
Ligc torso fleshl rib 3	490153	26
Ligc torso fleshl rib 4	490154	45
Ligc torso fleshl rib 5	490155	75
Ligc torso fleshl rib 6	490156	85
Ligc torso fleshl rib 7	490157	105
Ligc torso fleshl rib 8	490158	115
Ligc torso fleshl rib 9	490159	108
Ligc torso fleshl scapula	490160	160
Ligc torso fleshr clavicle	490161	72
Ligc torso fleshr costal 1	490162	7
Ligc torso fleshr costal 2	490163	23
Ligc torso fleshr costal 3	490164	25
Ligc torso fleshr costal 4	490165	31
Ligc torso fleshr costal 5	490166	35
Ligc torso fleshr costal 6	490167	159
Ligc torso fleshr rib 1	490168	1
Ligc torso fleshr rib 10	490169	93

Table A-2   List of parts containing beam elements (continued)

Part name	Part ID	No. of elements
Ligc torso fleshr rib 11	490170	72
Ligc torso fleshr rib 12	490171	29
Ligc torso fleshr rib 2	490172	15
Ligc torso fleshr rib 3	490173	26
Ligc torso fleshr rib 4	490174	45
Ligc torso fleshr rib 5	490175	75
Ligc torso fleshr rib 6	490176	85
Ligc torso fleshr rib 7	490177	105
Ligc torso fleshr rib 8	490178	115
Ligc torso fleshr rib 9	490179	108
Ligc torso fleshr scapula	490180	160
Ligl claviclec sternumA	490087	13
Ligl claviclel scapula	490045	250
Ligl rib 10l costal 6	490055	20
Ligl rib 10l rib 11	490077	87
Ligl rib 11l rib 12	490078	107
Ligl rib 1l costal 1	490046	20
Ligl rib 1l rib 2	490068	106
Ligl rib 2l costal 2	490047	24
Ligl rib 2l rib 3	490069	197
Ligl rib 3l costal 3	490048	17
Ligl rib 3l rib 4	490070	218
Ligl rib 4l costal 4	490049	18
Ligl rib 4l rib 5	490071	240
Ligl rib 5l costal 5	490050	15
Ligl rib 5l rib 6	490072	248
Ligl rib 6l costal 6	490051	16
Ligl rib 6l rib 7	490073	252
Ligl rib 7l costal 6	490052	17
Ligl rib 7l rib 8	490074	197
Ligl rib 8l costal 6	490053	17
Ligl rib 8l rib 9	490075	204
Ligl rib 9l costal 6	490054	19
Ligl rib 9l rib 10	490076	160
Ligl scapulal rib 1	490079	7
Ligl scapulal rib 2	490080	105
Ligl scapulal rib 3	490081	121
Ligl scapulal rib 4	490082	109
Ligl scapulal rib 5	490083	106
Ligl scapulal rib 6	490084	92
Ligl scapulal rib 7	490085	72
Ligl scapulal rib 8	490086	23
Ligr claviclec sternumA	490044	13
Ligr clavicler scapula	490000	250
Ligr rib 10r costal 6	490012	20
Ligr rib 10r rib 11	490034	87

Table A-2   List of parts containing beam elements (continued)

Part name	Part ID	No. of elements
Ligr rib 11r rib 12	490035	107
Ligr rib 1r costal 1	490003	20
Ligr rib 1r rib 2	490025	106
Ligr rib 2r costal 2	490004	24
Ligr rib 2r rib 3	490026	197
Ligr rib 3r costal 3	490005	17
Ligr rib 3r rib 4	490027	218
Ligr rib 4r costal 4	490006	18
Ligr rib 4r rib 5	490028	240
Ligr rib 5r costal 5	490007	15
Ligr rib 5r rib 6	490029	248
Ligr rib 6r costal 6	490008	16
Ligr rib 6r rib 7	490030	252
Ligr rib 7r costal 6	490009	17
Ligr rib 7r rib 8	490031	197
Ligr rib 8r costal 6	490010	17
Ligr rib 8r rib 9	490032	204
Ligr rib 9r costal 6	490011	19
Ligr rib 9r rib 10	490033	160
Ligr scapular rib 1	490036	7
Ligr scapular rib 2	490037	105
Ligr scapular rib 3	490038	121
Ligr scapular rib 4	490039	109
Ligr scapular rib 5	490040	106
Ligr scapular rib 6	490041	92
Ligr scapular rib 7	490042	72
Ligr scapular rib 8	490043	23

List of Symbols, Abbreviations, and Acronyms

1-D	1-dimensional
2-D	2-dimensional
ARL	US Army Research Laboratory
BABT	behind armor blunt trauma
CT	computed tomography
FE	finite element
NIJ	National Institute of Justice
NLV	nonlinear viscoelastic
PMHS	postmortem human subject
THUMS	Total Human Model for Safety

1	DEFENSE TECHNICAL
(PDF)	INFORMATION CTR
	DTIC OCA

2	DIR ARL
(PDF)	IMAL HRA
	RECORDS MGMT
	RDRL DCL
	TECH LIB

1	GOVT PRINTG OFC
(PDF)	A MALHOTRA

1	WAKE FOREST UNIVERSITY
(PDF)	K DANELSON

31	ARL
(PDF)	RDRL WM
	J ZABINSKI
	RDRL WMP
	D LYON
	RDRL WMP B
	C HOPPEL
	M KLEINBERGER
	T WEERASOORIYA
	K RAFAELS
	P J MCKEE
	S WOZNIAK
	J MCDONALD
	A EIDSMORE
	C WEAVER
	B FAGAN
	E MATHEIS
	K THOMPSON
	T ZHANG
	S ALEXANDER
	A GUNNARSSON
	A DAGRO
	T BAUMER
	RDRL WMP C
	S SATAPATHY
	A SOKOLOW
	RDRL WMP D
	R DONEY
	RDRL WMP F
	N GNIAZDOWSKI
	M TEGTMEYER
	R KARGUS
	D KRAYTERMAN
	J PRITCHETT
	A GOERTZ
	RDRL WMP G
	S KUKUCK
	R SPINK
	RDRL SLB W
	K LOFTIS